The Astronomical Journal, 164:239 (21pp), 2022 December https://doi.org/10.3847/1538-3881/ac9905

Roaring Storms in the Planetary-mass Companion VHS 1256-1257 b: Hubble Space Telescope Multiepoch Monitoring Reveals Vigorous Evolution in an Ultracool Atmosphere

Yifan Zhou[1,8], Brendan P. Bowler[1], Dániel Apai[2,3], Tiffany Kataria[4], Caroline V. Morley[1], Marta L. Bryan[5,9], Andrew J. Skemer[6], and Björn Benneke[7]
[1] Department of Astronomy, The University of Texas at Austin, 2515 Speedway, Stop C1400, Austin, TX 78712, USA; yifan.zhou@utexas.edu
[2] Department of Astronomy/Steward Observatory, The University of Arizona, 933 N. Cherry Avenue, Tucson, AZ 85721, USA
[3] Department of Planetary Science/Lunar and Planetary Laboratory, The University of Arizona, 1640 E. University Boulevard, Tucson, AZ 85718, USA
[4] Jet Propulsion Laboratory, California Institute of Technology, 4800 Oak Grove Drive, Pasadena, CA, USA
[5] Department of Astronomy, University of California Berkeley, Berkeley, CA 94720-3411, USA
[6] Department of Astronomy, University of California Santa Cruz, 1156 High Street, Santa Cruz, CA, USA
[7] University of Montreal, Montreal, QC, H3T 1J4, Canada
Received 2022 January 7; revised 2022 October 1; accepted 2022 October 3; published 2022 November 7

Abstract

The photometric and spectral variability of brown dwarfs probes heterogeneous temperature and cloud distributions and traces the atmospheric circulation patterns. We present a new 42 hr Hubble Space Telescope (HST) Wide Field Camera 3 G141 spectral time series of VHS 1256-1257 b, a late L-type planetary-mass companion that has been shown to have one of the highest variability amplitudes among substellar objects. The light curve is rapidly evolving and best fit by a combination of three sine waves with different periods and a linear trend. The amplitudes of the sine waves and the linear slope vary with the wavelength, and the corresponding spectral variability patterns match the predictions by models invoking either heterogeneous clouds or thermal profile anomalies. Combining these observations with previous HST monitoring data, we find that the peak-to-valley flux difference is $33\% \pm 2\%$ with an even higher amplitude reaching 38% in the *J* band, the highest amplitude ever observed in a substellar object. The observed light curve can be explained by maps that are composed of zonal waves, spots, or a mixture of the two. Distinguishing the origin of rapid light curve evolution requires additional long-term monitoring. Our findings underscore the essential role of atmospheric dynamics in shaping brown-dwarf atmospheres and highlight VHS 1256-1257 b as one of the most favorable targets for studying the atmospheres, clouds, and atmospheric circulation of planets and brown dwarfs.

Unified Astronomy Thesaurus concepts: Brown dwarfs (185); L dwarfs (894); Atmospheric variability (2119); Planetary atmospheres (1244); Spectroscopy (1558); Time series analysis (1916); Atmospheric circulation (112); Atmospheric clouds (2180)

Supporting material: data behind figure

1. Introduction

Brown dwarfs and wide-orbit (>100 au) planetary-mass companions (PMC) are often regarded as analogs to gas giant planets because they share similar effective temperatures, thermal profiles, and atmospheric compositions (e.g., Beichman et al. 2014; Chabrier et al. 2014; Faherty et al. 2016; Bowler et al. 2017; Zhang et al. 2021). Without bright host stars contaminating the signals from the companions, observations of brown dwarfs and PMCs have delivered exquisite photometry, spectra, and time-series data that enable comprehensive atmospheric studies (e.g., Miles et al. 2020; Vos et al. 2020, 2022; Apai et al. 2021; Best et al. 2021; Burningham et al. 2021). These objects are valuable targets for understanding the substellar atmospheric dynamics. Their high internal heat flux and fast rotation rates lead to intense thermal heating and strong Coriolis forces that define unique circulation regimes (Zhang & Showman 2014; Showman et al. 2019, 2020; Tan & Showman 2021a, 2021b).

Driven by circulation, atmospheric structures form in substellar atmospheres and evolve over time. Heterogeneous distributions of condensate clouds and thermal profiles cause brightness and spectroscopic variability (e.g., Morley et al. 2014; Robinson & Marley 2014; Tremblin et al. 2020), which has been found in a large number of brown dwarfs and a handful of PMCs (e.g., Artigau et al. 2009; Radigan et al. 2012; Buenzli et al. 2014a; Metchev et al. 2015; Zhou et al. 2016; Vos et al. 2017, 2020, 2022; Eriksson et al. 2019; Zhou et al. 2019; Bowler et al. 2020; Tannock et al. 2021). Two types of variability patterns have emerged in observations, and they offer distinctive evidence for circulation shaping the atmospheres. The first type is rotational modulations, manifesting as periodic and often (approximately) sinusoidal light curves (e.g., Apai et al. 2013; Vos et al. 2017; Biller et al. 2018; Tannock et al. 2021). This type of variability originates from a brown dwarf's rotation transporting temperature and cloud anomalies in and out of the visible hemisphere, and hence the light curve constrains the object's rotation period despite the possible minor influence of differential rotation (e.g., Metchev et al. 2015; Scholz et al. 2015; Zhou et al. 2016; Tannock et al. 2021). The size and shape of the atmospheric structures

[8] 51 Pegasi b Fellow.
[9] NHFP Sagan Fellow.

determine the appearance of the light curve, and thus high-precision time-series observations enable the reconstruction of top-of-atmosphere maps (Apai et al. 2013; Karalidi et al. 2015, 2016). The size of the retrieved spots constrains wind speeds in brown-dwarf atmospheres based on Rhines' length argument (Rhines 1975; Showman & Guillot 2002). Combining periods measured at infrared (IR) and radio wavelengths, which trace the stratospheric and magnetospheric rotation rates, Allers et al. (2020) directly measured the wind speed of a brown dwarf. Amplitudes and phase offsets of rotational modulations often vary with the wavelength (e.g., Buenzli et al. 2012; Lew et al. 2016; Yang et al. 2016; Biller et al. 2018), and the observed wavelength dependence of the modulations supports a picture in which heterogeneous clouds are the primary source of variability in L/T transition dwarfs (e.g., Apai et al. 2013; Buenzli et al. 2014b; Lew et al. 2020).

The second type of variability is the long-term and irregular light curve evolution. Artigau et al. (2009) and Radigan et al. (2012) discovered significant morphological differences between light curves separated by a few rotation periods. Metchev et al. (2015) found that irregular changes were common among a large sample of brown-dwarf light curves collected by the Spitzer Space Telescope. So far, the most comprehensive observational evidence of brown-dwarf light curve evolution is from long-time baseline brown-dwarf monitoring campaigns conducted with Spitzer and the Transiting Exoplanet Survey Satellite (by Apai et al. 2017 and Apai et al. 2021, respectively). In these studies, light curves spanning over one hundred brown-dwarf rotation periods exhibited a wealth of patterns, including sinusoids, beating of two similar frequencies, and irregular and nonperiodic variations. The evolution of these patterns is hardly predictable: they may maintain a regular sine-wave shape in a short time interval but then evolve dramatically over just a few rotations. Apai et al. (2017, 2021) found that the circular/elliptical spot models alone could not explain several evolving light curves. On the other hand, the planetary-scale wave model, which is supported by the general circulation model (GCM) results (e.g., Showman et al. 2019; Tan & Showman 2021b), fits observations much better.

Despite this progress, a fundamental question remains: what are the physical mechanisms that lead to the heterogeneous atmospheres and long-term atmospheric evolution of brown dwarfs? This question has been explored in several studies modeling the circulation patterns in these atmospheres. The vigorous convection of a brown dwarf can perturb its stratosphere and introduce inhomogeneity in the temperature and thermal profile distributions (Showman & Kaspi 2013; Robinson & Marley 2014). Meanwhile, because the thermal profile of a brown dwarf intercepts the condensation curves of Fe and Si minerals, these species condense and coagulate into clouds (e.g., Ackerman & Marley 2001; Marley et al. 2002, 2013; Burrows et al. 2006; Helling et al. 2008; Charnay et al. 2018; Gao et al. 2018). Circulation regularizes cloud formation, carving clouds into patches (e.g., Showman & Kaspi 2013). By tuning the GCM simulations to match the properties of typical brown dwarfs, Showman et al. (2019) found that zonal bands and jets are common outcomes. Furthermore, under the condition of short drag and radiative timescales, planetary-scale waves induce long-term oscillations in a brown-dwarf stratosphere. These oscillations are similar to those observed on Earth, Jupiter, and Saturn. Moreover, due to cloud radiative feedback, cloud thickness and the surrounding thermal profile can modulate spontaneously, introducing quasiperiodic variability that does not correlate with rotation (Tan & Showman 2019). Tan & Showman (2021a, 2021b) further integrated cloud radiative feedback into GCMs and found that the vigorous atmospheric circulation triggered and maintained by cloud formation can substantially impact the observable properties of brown dwarfs. The types of heterogeneous atmospheres can be identified by spectral variability (Morley et al. 2014), and the circulation models can be probed through light curve morphology and variability timescales (e.g., Zhang & Showman 2014; Tan & Showman 2021b). High-precision, multiwavelength, and multiepoch time-resolved observations provide the most thorough and direct way to test these models.

VHS J125060.192-125723.9 b (hereafter, VHS 1256 b), an L7 brown-dwarf companion hosted by a late-M equal-mass binary (Gauza et al. 2015; Stone et al. 2016), is an excellent target for such observations. Immediately after its discovery, it became a target of interest for atmospheric studies because of its likely young age (<300 Myr; Gauza et al. 2015), low surface gravity, red infrared colors, and spectral resemblance to directly imaged planets such as HR 8799 bcde. Follow-up observations have found that VHS 1256 b's atmosphere has thick condensate clouds (e.g., Rich et al. 2016) and a low methane abundance that deviates from the expected value based on chemical equilibrium (Miles et al. 2018). By comparing the luminosity of VHS 1256 b with evolutionary tracks, Dupuy et al. (2022) found the companion's mass to be $11.8 \pm 0.2 M_{\rm Jup}$ or $16 \pm 1 M_{\rm Jup}$, depending on the model choices. It is also among the first targets to be observed by JWST as part of an Early Release Science program (Hinkley et al. 2022). In time-resolved observations, VHS 1256 b has exhibited high amplitude brightness and spectral variability (e.g., Bowler et al. 2020; Zhou et al. 2020). The host binary stars show low-level (<0.3%) photometric modulations (Miles-Páez 2021).

The variability signals in VHS 1256 b revealed insightful information about its atmosphere. Bowler et al. (2020) conducted time-resolved observations of VHS 1256 b with the Hubble Space Telescope (HST) Wide Field Camera 3 (WFC3) G141 grism in 2018. The six-orbit continuous monitoring (~9 hr) resulted in a light curve that spanned less than half of its rotation period. At this epoch, VHS 1256 b's 1.1–1.7 μm band-integrated light curve exhibited a 19.3% peak-to-valley brightness change, the second highest ever found in a brown dwarf. Shortly after this discovery, a 38 hr Spitzer/IRAC 4.5 μm campaign was conducted to recover the companion's full rotation period (Zhou et al. 2020). This follow-up observation found a sinusoidal light curve that helped determine a precise period of 22.02 ± 0.04 hr. Zhou et al. (2020) interpreted this measurement as the rotation period of VHS 1256 b. The combined spectral variability in the 1.1–1.7 μm WFC3/G141 band and the 4.5 μm Spitzer band agreed with predictions from partly cloudy models (Morley et al. 2014).

In this paper, we present a new set of HST/WFC3 spectroscopic light curves of VHS 1256 b collected in 2020. The new observations have a time baseline of 42 hr, covering approximately two rotation periods of VHS 1256 b. Combining these new data with the 2018 HST results probes the companion's long-term changes on a timescale of nearly ~900 rotation periods, offering a detailed view of VHS 1256 b's stormy atmosphere. This paper is organized as follows: we describe the observations and the data reduction method in

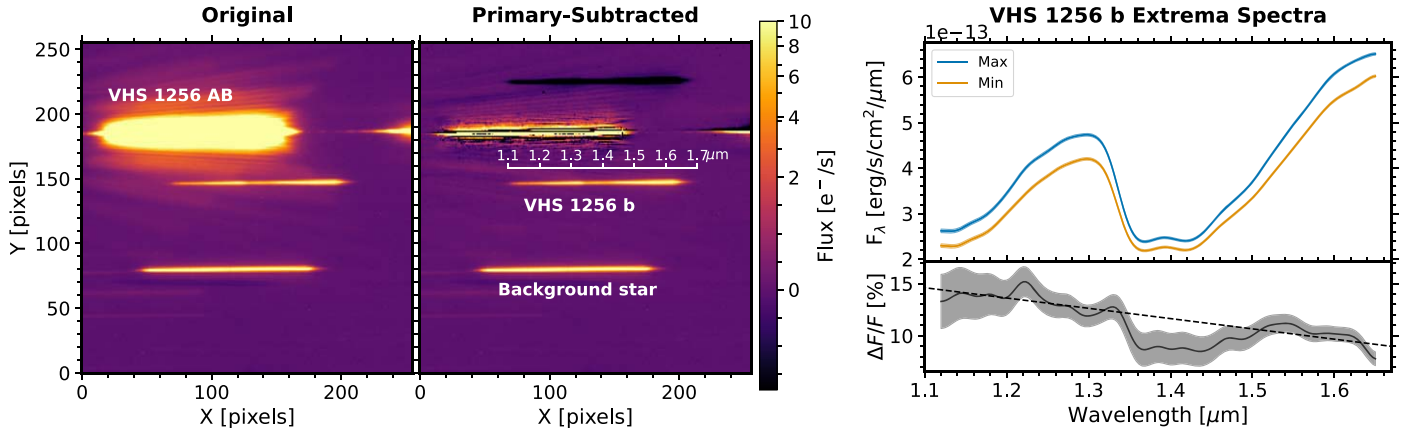

Figure 1. Median-combined original (left) and primary-subtracted (middle) images of the Epoch 2020 observations, and extracted spectra of VHS 1256 b (right) at maximum and minimum brightness. In the left panel, from top to bottom, the three brightest spectral traces are VHS 1256 AB (the host binary), VHS 1256 b (the substellar companion), and a background star (2MASS J12560179–1257390). The VHS 1256 b trace is moderately contaminated by the primary PSF. We mitigate the contamination by subtracting an empirically derived PSF model, and the primary-subtraction result is shown in the middle panel. The right panel shows the extracted spectra of VHS 1256 b at its brightest (blue) and faintest (yellow) phases. Their relative difference and the uncertainty are shown as a black line and a gray shaded region in the bottom subplot of the right panel.

Section 2, present the immediate results from the 2020 campaign in Section 3, and analyze the long-term changes between the 2018 and 2020 epochs in Section 4. Then in Section 5, we discuss the rotation period measurement, the atmospheric circulation patterns, and the unusually high variability amplitude of VHS 1256 b. We summarize our results and conclude in Section 6.

2. Observations and Data Reduction

We conducted spectroscopic monitoring of VHS 1256 b using the HST/WFC3 IR Channel for 15 orbits from UT 2020 May 26 09:27:17 to 2020 May 28 03:29:24 (Program ID: GO-16036, PI: Zhou; hereafter, we refer to this program as "Epoch 2020"). Prior to this program, our target was observed with the same instrument for six continuous orbits from UT 2018 March 5 16:02:30 to 2018 March 6 00:42:47 (Program ID: GO-15197, PI: Bowler, results are published in Bowler et al. 2020; hereafter, we refer to this program as "Epoch 2018").

The overall design of the two observing campaigns are identical. Each orbit started with two to four direct-imaging exposures in the F132N filter for wavelength calibration. Eleven 223 s spectroscopic frames in the G141 grism then followed. The spectrograph has a spectral resolution of $R \sim 130$ at 1.4 μm and a wavelength range spanning from 1.12 to 1.65 μm. The median-combined spectral image obtained in the Epoch 2020 observations is shown in the left panel of Figure 1 with the spectral trace of VHS 1256 b in the middle and two nearby sources above (VHS 1256–1257 AB) and below (background star 2MASS J12560179–1257390).

In two respects, the Epoch 2020 campaign differs from the Epoch 2018 one. First, the 2020 campaign has a longer time baseline. The purpose was primarily to monitor the brown-dwarf companion for multiple rotations. For optimal time coverage and scheduling flexibility, we divided the observations into four segments. The first segment contained nine consecutive orbits tracking high-cadence (with a rate of 242 s per frame) variability for 13.4 hr, approximately 60% of VHS 1256 b's 22.0 hr rotation period ($P_{\rm rot}$). After a gap of five orbits, three two-orbit segments followed with gaps of two and four orbits separating them. These three short segments significantly extended the overall time baseline. As a result, the entire campaign spanned 42.0 hr or 1.91 $P_{\rm rot}$ of VHS 1256 b.

Second, the position angles (PAs) of HST are different between the two campaigns: $\mathrm{PA}_{2020} = 299.^\circ0$ and $\mathrm{PA}_{2018} = 143.^\circ1$.[10] This difference is due to the fact that the allowed telescope PAs were set as ranges instead of fixed values.

The PA orientation of the Epoch 2020 observations was less optimal than that in the Epoch 2018 observations, resulting in a smaller projected separation between the spectral traces of VHS 1256 b and VHS 1256 AB on the detector (38 pixels in Epoch 2020 versus 57 pixels in Epoch 2018). The proximity between the two traces caused modest contamination from the host binary's point-spread function (PSF) at the position of the companion (Figure 1). Therefore, primary subtraction is necessary for accurately extracting spectra from the Epoch 2020 data.

We adopt a "flip-and-subtract" approach to remove contaminating flux. It includes four steps:

1. Construct an empirical PSF template by median-combining all sky-subtracted spectroscopic images.
2. Flip the template upside down (i.e., mirror the image with respect to the x-axis); shift and tilt the flipped template to align the template spectral trace with the one in observed images; and linearly scale the template to match the flux with the observed spectral trace.
3. Subtract the flipped template from the target image and calculate the sum of squared residuals in an optimization region. This is chosen to be a 15×140 rectangle 20 pixels above VHS 1256 b's trace.
4. Optimize the shift distance, tilt angle, and scaling factor by minimizing the sum of squared residuals. After the optimal values were found, use them to derive the final primary-subtracted images.

The middle panel in Figure 1 shows an example of primary-subtracted images. After subtraction, the contamination, measured as the average flux in the optimization region, is below the average sky background and hence does not cause

[10] Following the definition used in the WFC3 Instrument Handbook (https://hst-docs.stsci.edu/wfc3ihb) and FITS file headers, these angles refer to the PA of HST's V3 axis.

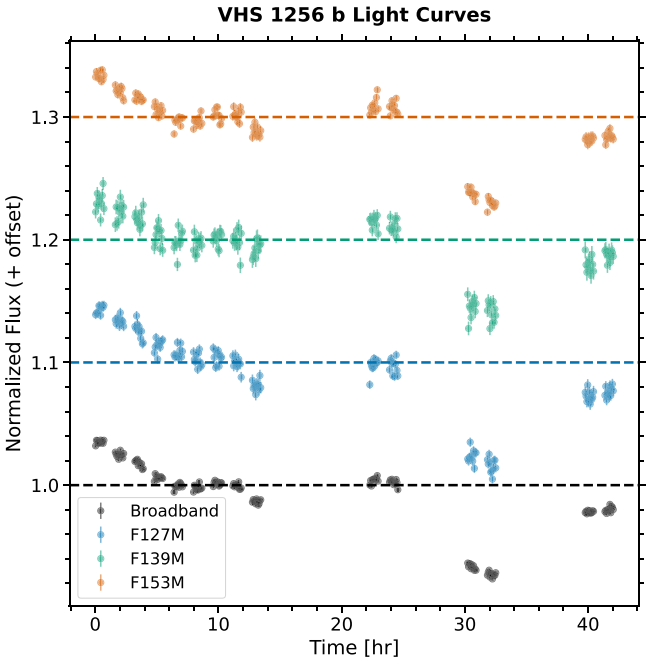

Figure 2. Light curves of VHS 1256 b integrated in four representative bandpasses obtained in the 2020 observations: the G141 broad band (black), the F127M filter (blue), the F139M filter (green), and the F153M filter (red). High amplitude brightness modulations are detected in every light curve.

significant uncertainties in photometry. We proceeded to use the primary-subtracted images to extract the spectra of VHS 1256 b.

The remaining data reduction procedures are identical to those detailed in Bowler et al. (2020). In the following section, we discuss VHS 1256 b's atmospheric properties based on its spectra and light curves presented in Figures 1 and 2, respectively.

3. Results

3.1. Light Curve Analysis

Figure 2 shows the normalized light curves of VHS 1256 b during the Epoch 2020 observations in four representative bands: the G141 bandpass (1.12–1.65 μm), the F127M filter (centered at VHS 1256 b's J-band peak, $\lambda = 1.27$ μm, FWHM = 0.069 μm), the F139M filter (sensitive to water absorption, $\lambda = 1.38$ μm, FWHM = 0.065 μm), and the F153M filter (continuum emission on the red side of the water absorption band $\lambda = 1.53$ μm, FWHM = 0.069 μm). High amplitude modulations are present in all light curves. Unlike the Epoch 2018 light curves that were well fit by single sinusoids (Bowler et al. 2020; Zhou et al. 2020), the Epoch 2020 light curves exhibit irregular structures.

We seek the simplest model that recovers the four band-integrated light curves. Following Apai et al. (2017, 2021), we construct a model by summing multiple sinusoids and set the periods of all sinusoids to be free parameters. When the periods are harmonics, this model becomes a truncated Fourier series. In addition to sinusoids, we include a linear term to encapsulate the long-term atmospheric changes of which the timescales significantly exceed the observing window (e.g., Biller et al. 2018).

An N-component multisinusoidal model is expressed as

$$F(t) = C_0 + C_1 t + \sum_i^N (A_i \sin(2\pi t/P_i) + B_i \cos(2\pi t/P_i)), \quad (1)$$

where A_i and B_i are the amplitudes of the ith order sine and cosine components, respectively. C_0 is a normalization factor, and $C_1 t$ is the linear trend. There are $3N + 2$ free parameters.

We incrementally increase N and use the maximum likelihood method to find the best-fitting A_i, B_i, and P_i. The likelihood function is defined as:

$$\mathcal{L} = \prod_j^n \frac{1}{\sqrt{2\pi\sigma_j^2}} \exp\left(-\frac{(f_j - F(t_j))^2}{2\sigma_j^2}\right), \quad (2)$$

where f_j, σ_j, and t_j are the normalized flux density, the uncertainty, and the time stamp of the jth data point. We assume uninformative (uniform) priors for the free parameters and fit the model by sampling the posterior probability function using Markov Chain Monte Carlo (implemented by `emcee`; Foreman-Mackey et al. 2013). For model selection, the Bayesian information criterion (BIC) is used. It is derived as

$$\mathrm{BIC} = \chi^2 + k \ln(n), \quad (3)$$

in which χ^2, k, and n are the nominal chi-square values between the model and the data, the number of free parameters, and the number of data points, respectively. The fitting statistics are listed in Table 1.

We determine the truncation order N based on the BIC values with $\Delta\mathrm{BIC} > 10$ as the threshold for favoring a more complex model (e.g., Kass & Raftery 1995). For all four light curves, the $N = 3$ models are favored over any of the simpler models. For the broadband and F153M light curves, the even more complex $N = 4$ model is preferred. However, because the $N = 4$ model is not supported in all cases, we select the simpler $N = 3$ model for the subsequent analysis.

Our best-fitting model is presented in Figure 3 and the posterior distributions of the model parameters are shown in Figure 4. Based on the broadband light curve fit, the three sine waves have periods of: 18.8 ± 0.2 hr (Wave 1), 15.1 ± 0.2 hr (Wave 2), and 10.6 ± 0.1 hr (Wave 3). The peak-to-peak amplitudes of the three waves are $5.8\% \pm 0.8\%$, $4.6\% \pm 0.7\%$, and $1.4\% \pm 0.1\%$. Waves 1 and 2 form a beating pattern, and Wave 3 has a period close to one half of the 22 hr period best fit to the Spitzer 4.5 μm light curve. In Figure 3, we decompose the model and visualize how each component contributes to the observed light curve evolution. In the first half, Waves 1 and 2 are in nearly opposite phases, and they cancel each other out. In the same segment, the modulations are mostly from Wave 3 and the linear trend. In the second half, Waves 1 and 2 start to align in phase and jointly increase the total modulation amplitude. Notably, the periods of the first two waves are significantly shorter than the one best fit to VHS 1256 b's Spitzer light curve (22.04 hr, Zhou et al. 2020). We discuss the discrepancy of the period measurements in Section 5.1.

Our light curves can be equally well fit by a Fourier series truncated at the fourth order with a base-order period of 41.4 hr combined with a linear trend. This truncated Fourier series has the same number of free parameters as our best-fitting model. For the broadband light curve, the four Fourier components have peak-to-peak amplitudes of 1.74%, 4.14%, 2.92%, and 0.90% for orders 1 to 4, respectively. Components 2 to 4 ($P_2 = 20.7$ hr, $P_3 = 13.8$ hr, $P_4 = 10.4$ hr) mimic the behaviors of Waves 1 to 3 in the multisinusoidal model while the base-order component contributes little for recovering the observed modulations. The period of the base order far exceeds the

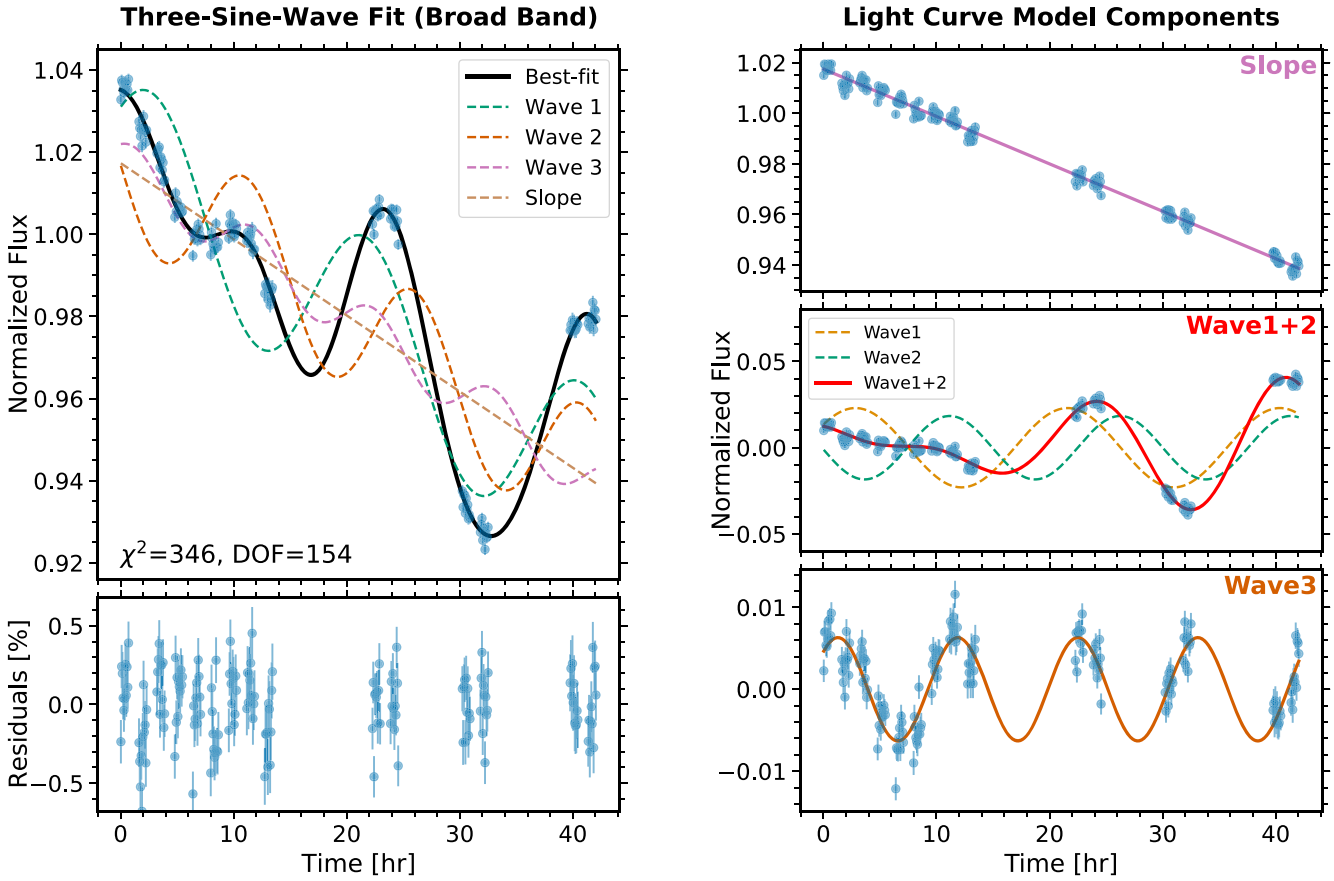

Figure 3. Fitting the multiple-sinusoidal model to the broadband light curve. The left panel highlights the excellent agreement between the observed broadband light curve (blue dots) and the best-fitting model (black solid line). Individual model components (the three sine waves and the linear trend) are shown as color dashed lines. In the right panel, we isolate these components to illustrate their importance to the good fit. The top, middle, and bottom panels feature the linear slope, Waves 1+2 and Wave 3, respectively. In each panel, model components other than the one being highlighted are subtracted from both the observed and model light curves. The middle-right panel demonstrates the combined effect of two sine waves that have best-fitting periods of 18.8 and 15.1 hr. In this panel, individual waves are plotted in the dashed lines, and their sum is in the solid red line.

Table 1
χ^2 and BIC Values in Light Curve Fittings

N	DOF	Broad Band			F127M			F139M			F153M		
		χ^2	BIC[a]	ΔBIC[b]	χ^2	BIC	ΔBIC	χ^2	BIC	ΔBIC	χ^2	BIC	ΔBIC
1	160	5580	−26602		1562	−4103		442.8	−1644		1444	−6364	
2	157	686.7	−31480	4878	335.9	−5314	1211	260.9	−1811	167	381	−7411	1047
3	154	345.9	−31806	326	280.0	−5354	40	229.9	−1826	15	291	−7487	76
4	151	291.2	−31845	41	272.3	−5346	−8	229.4	−1812	−14	262	−7500	13
Favored N			4			3			3			4	

Notes.
[a] BIC values are relative to those for the best-fitting linear trend.
[b] ΔBIC is the BIC decrease due to adding one sinusoid. When ΔBIC > 10, the more complex model is favored.

rotation period of VHS 1256 b and is thus not physical. When we limit the base-order period below 25 hr, a conservative boundary set based on the 22.0 hr period measured in the Spitzer light curve, the truncated Fourier series does not provide a good fit to the observations.

3.2. Lomb–Scargle Periodogram Analysis

To further interpret the periodic signals, we conducted a Lomb–Scargle (Lomb 1976; Scargle 1982) periodogram analysis using the `LombScargle` module in the `astropy` package (Robitaille et al. 2013) with the `fit_mean` option turned on (see, e.g., Zechmeister & Kürster 2009 and VanderPlas 2018 and the references therein). The results are shown in Figure 5. Due to the irregular observing windows and a mixture of multiple periodic signals in VHS 1256 b's light curves, periods from fitting Equation (1) do not match the peak positions in the periodogram. To understand this mismatch, we computed several illustrative periodograms and compare them

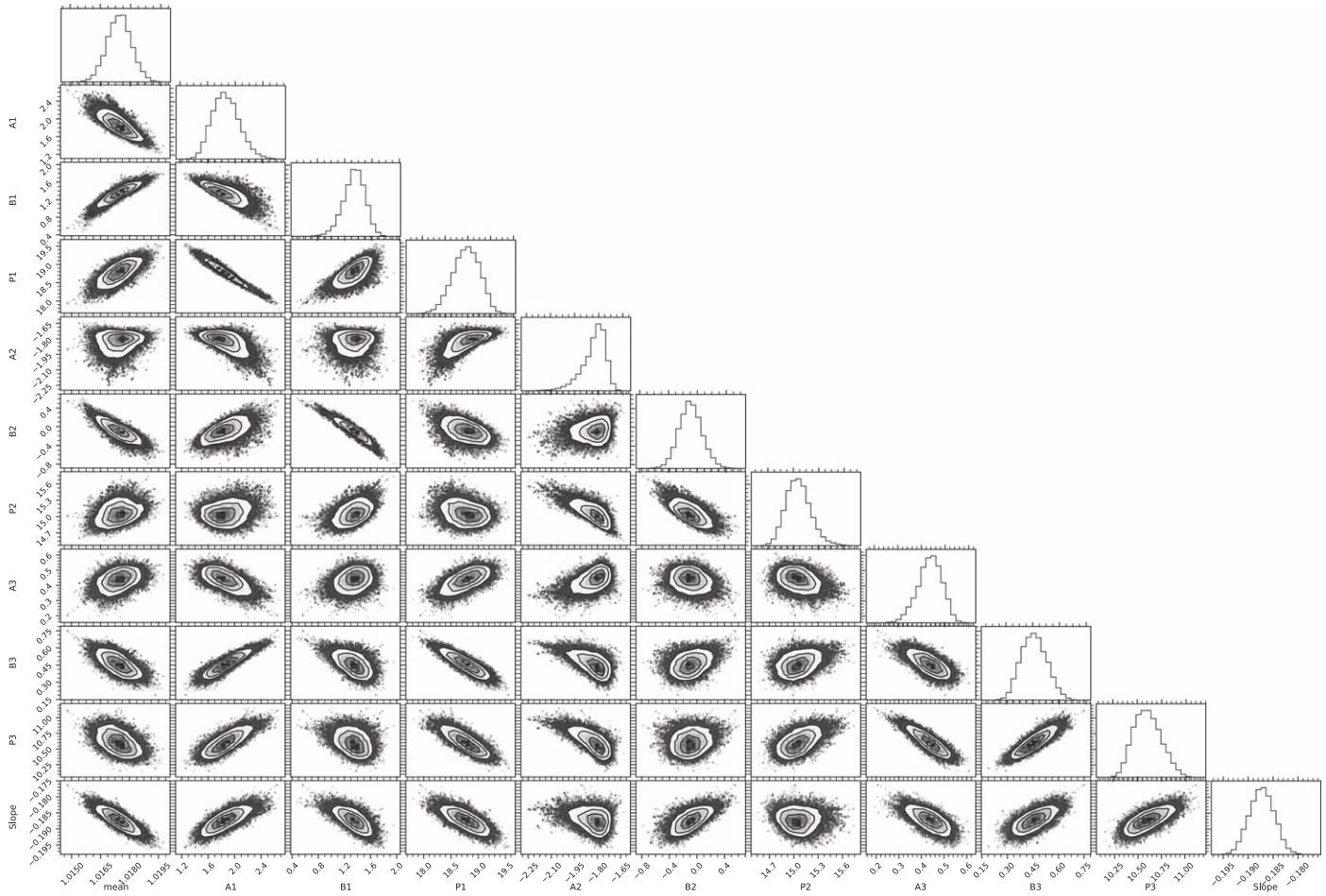

Figure 4. Posterior distributions of the three-sine-wave parameters in a corner plot.

with the one derived using the observed light curve. These additional periodograms are for:

1. The window function: an evenly sampled Boolean series with 1 for visible windows and 0 for gaps.
2. The oversampled best-fitting model: a uniform grid oversampled by 100× and limited to a 42 hr window containing the observations.
3. The oversampled best-fitting model with a long baseline: a uniform grid oversampled by 100× and limited to a 210 hr window.
4. The realistically sampled best-fitting model: sampled in the same manner and spanning the same time baseline as the observations.

These periodograms are presented in Figure 5. The top panel shows the window function effect. By comparing the periodograms of the observed light curve and the window function, we find that HST's visibility cycle induces a series of peaks near 96 minutes onto both periodograms. The middle panel shows that the limited observing time baseline combined with a mixture of multiple periodic signals can further confuse the periodogram. The same panel highlights the periodograms of two well-sampled best-fitting multiple-sinusoidal models with different lengths, 42 hr (the same as the observations) and 210 hr (5× the observation baseline). While the 210 hr periodogram exhibits the three peaks accurately, the 42 hr periodogram only detects the 18.6 hr periodic signal but fails for the other two shorter and weaker modulations. In the bottom panel, when the model light curve is sampled in the same manner as the observations, its periodogram regresses to exactly the same pattern as the observed one, which includes false-positive peaks near 7 and 11 hr.

The Lomb–Scargle periodogram of an irregularly sampled light curve that contains multiple periodic signals may contain false detections. As a result, systematic uncertainties in period measurement can significantly exceed the least-squares errors (see Section 5.1).

3.3. Spectral Variability Analysis

The wavelength-dependent variability is perceptible by a visual inspection. Between the maximum and minimum spectra (right panel of Figure 1), the relative flux difference decreases in the H_2O band around 1.4 μm. A comparison of light curves between the F127M, F139M, and F153M bands (Figures 2 and 6) reveals a more subtle spectral variation. In the first segment ($t < 12$ hr), in which Waves 1 and 2 are in approximately opposite phases, the F127M light curve is nearly a straight line, but the F139M and the F153M curves exhibit upward curvatures between $t = 6$ hr and 12 hr, suggesting that Wave 3 is more significant at longer wavelengths.

To quantify these findings, we fit the three-sine-wave model to the spectroscopically resolved light curves. These light curves are obtained from 30 wavelength bins evenly split the 1.12–1.65 μm range (bin size: $\Delta\lambda = 0.018$ μm). In the

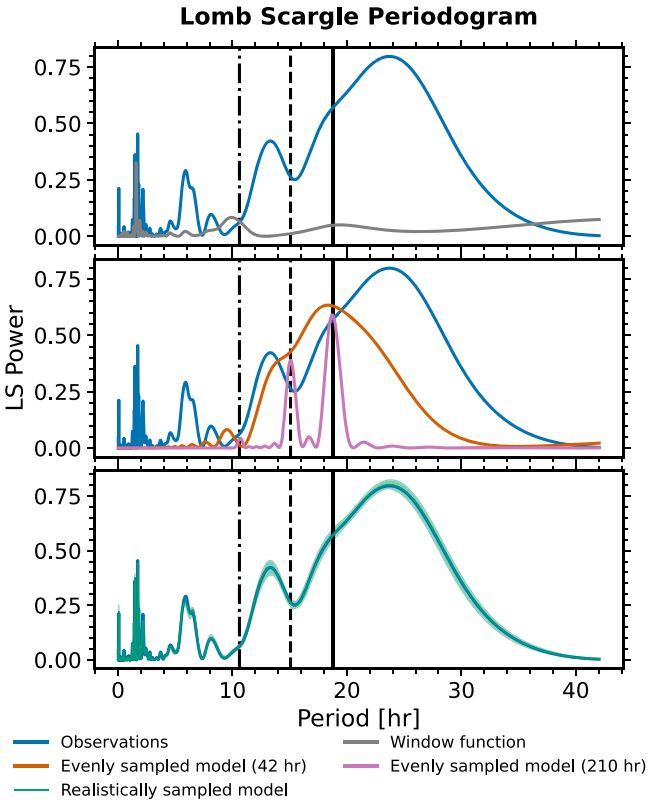

Figure 5. Results of the Lomb–Scargle periodograms analysis. The periodogram of the observed light curve (with the linear trend removed) is shown in all three panels as blue solid lines. In the top panel, the gray solid line marks the periodogram of the observing-window function. The middle panel includes two periodograms derived from the evenly sampled best-fitting model, with time ranges of 42 hr (orange) and 210 hr (magenta). In the bottom panel, the green shaded region shows the periodogram of the best-fitting model sampled in the same way as observations. The range of the region reflects fitting uncertainties. Due to the irregular sampling window, peak locations in the periodograms do not match the results obtained by fitting Equation (1) (black vertical lines).

spectroscopically resolved fits, the periods of the three sine waves are fixed to the values that best fit to the broadband light curve. The amplitudes, phase offsets, and the linear slope are left as free parameters. The best-fitting parameters are determined in the identical manner as the broadband light curve fits.

We find that the amplitudes of the three waves and the linear slope vary significantly with the wavelength, but none of the waves show any chromatic changes in the phase offsets. Figure 7 shows the amplitudes as a function of the wavelength for Waves 1 to 3 as well as the linear slope. Two patterns are revealed. The amplitudes of Waves 1 and 2 and the slope of the linear trend decrease in the 1.4 μm H_2O band. This spectral variability pattern has been identified in a handful of L/T transition dwarfs (e.g., Apai et al. 2013; Yang et al. 2014; Zhou et al. 2018), in red late L-type dwarfs (e.g., Lew et al. 2020), and in VHS 1256 b in its Epoch 2018 observations (Bowler et al. 2020; Zhou et al. 2020). The amplitude reduction in the H_2O band has been reproduced by partly cloudy models where the optical depths of the Fe and Si clouds are greater in the continuum than in the H_2O absorption band (Morley et al. 2014).

The amplitude of Wave 3 shows an opposite wavelength dependence and increases in the H_2O band. Based on atmospheric models, this signal may indicate the presence of thermal profile anomalies (Morley et al. 2014; Robinson & Marley 2014). In these models, the anomalous thermal profile (T-P) contains a constant displacement above a pressure threshold. This local T-P variation affects the strength of molecular absorption more than the continuum and create greater modulations in the absorption bands. Thermal profile anomalies were put forward to explain the spectral modulations of the T6 dwarf 2MASS J22282889-4310262 in which the continuum and H_2O bands modulate in opposite phases (Buenzli et al. 2012; Robinson & Marley 2014).

3.4. Comparing the Observed Spectral Variability with Models

In Bowler et al. (2020) and Zhou et al. (2020), the partly cloudy model successfully reproduced VHS 1256 b's spectral variability observed in the Epoch 2018 data. This model consists of two hemispheres with different cloud optical depths relative to the fully cloudy model (τ_c). The less cloudy hemisphere has a τ_c of 75% of the fully cloudy optical depth and the more cloudy hemisphere has a τ_c of 90%. All other parameters are identical to those best fit to the mean spectrum ($T_{\rm eff} = 1000$ K, $\log g = 3.2$, $f_{\rm sed} = 1.0$, and $\tau_c = 80\%$). Here, we compare this model with the spectral variability curves of Waves 1, 2, and the linear slope.

To allow the overall amplitudes to vary to fit the observations, we introduce covering fractions of the less cloudy ($\tau_c = 75\%$) and the more cloudy ($\tau_c = 90\%$) patches as free parameters. Then, the model's maximum and minimum spectra are:

$$S_{\rm max} = f_1 S_{\tau_c 75} + (1 - f_1) S_{\tau_c 80}, \quad (4)$$

$$S_{\rm min} = f_2 S_{\tau_c 90} + (1 - f_2) S_{\tau_c 80}, \quad (5)$$

where $S_{\tau_c 75}$, $S_{\tau_c 80}$, and $S_{\tau_c 90}$, represent the model spectra for $\tau_c = 75\%$, 80%, and 90%, respectively; f_1 and f_2 are the covering fractions of the $\tau_c = 75\%$ and 90% patches. The predicted semi-amplitude is

$$\Delta F/F = (S_{\rm max} - S_{\rm min})/(S_{\rm max} + S_{\rm min}). \quad (6)$$

We fit the output of Equation (6) to the observed spectral variability curves of Waves 1, 2, and the linear slope and show the results in Figure 7. The model reproduces the overall trends, including the reduced amplitudes in the water band and the decrease in amplitudes at longer wavelengths, but does not fit the observed curves perfectly. In particular, the partly cloudy model overpredicts the difference between the water band and the continuum. This result confirms that Waves 1, 2, and the slope trace the change of cloud optical depths. However, our untuned atmospheric model does not completely characterize the clouds of VHS 1256 b.

We also compare a Morley et al. (2014) hot-spot model to the spectral variability curve of Wave 3. In this model, extra energy is injected at $P = 10$ bar with a Chapman heating function to elevate the thermal profile above this pressure level in one hemisphere. In the other hemisphere, the thermal profile is kept in the form determined by radiative–convective equilibrium. The spectra of the two hemispheres and the corresponding spectral variability curve are derived using Equations (4) and (6). We allow the model $\Delta F/F$ curve to scale linearly to fit the observed results. The scaling corresponds to the covering fraction change of the spot. As shown in the bottom left panel of Figure 7, the model matches the observed curve well, supporting that Wave 3 probes a heterogeneous distribution of thermal profiles.

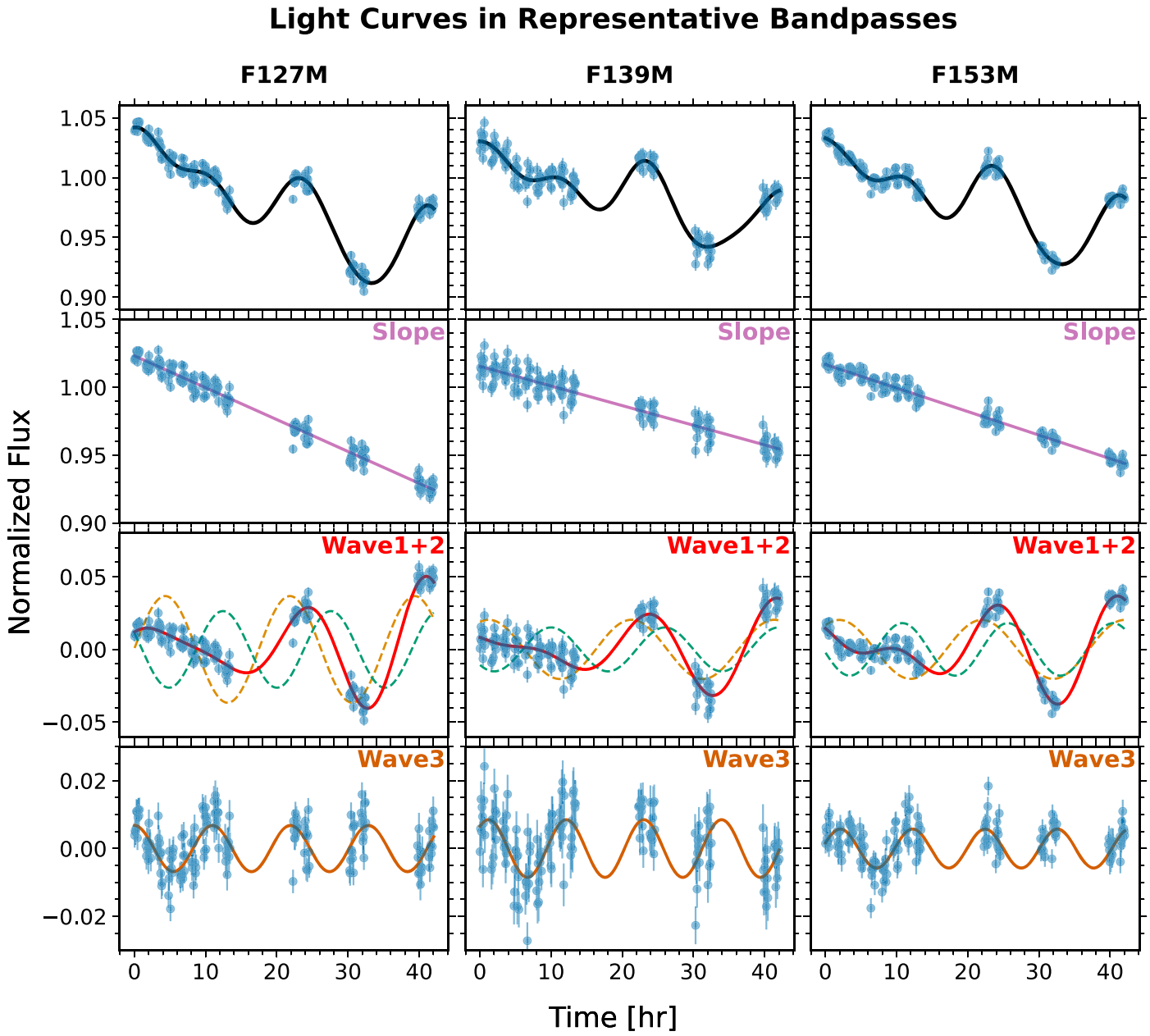

Figure 6. Fitting the multiple-sinusoidal model to light curves integrated in representative bandpasses. The three bandpasses represent the 1.4 μm water absorption band (F139M, middle column) and the continuum (F127M, left column; F153M, right column). The markers are identical to those in Figure 3. The top row shows the comparisons between the model and observed light curves, and rows 2–4 illustrate the individual components. In each row, the y-axis scale is kept consistent for all columns, allowing crude visual comparisons between light curves (e.g., the F127M light curve has a steeper slope and high Wave 1 and 2 amplitudes; the F139M light curve has the highest Wave 3 amplitude).

4. Long-term Light Curve Evolution

The two epochs of HST observations of VHS 1256 b enable an investigation of its spectral variability on the 1–2 yr timescale. In this section, we conduct a joint analysis of the two spectral time-series data sets. This includes: (1) consistently reducing the two epochs of data; (2) evaluating cross-epoch flux differences; (3) estimating errors in cross-epoch flux calibration; and (4) interpreting the spectral variability of VHS 1256 b between the two epochs.

4.1. Consistent Data Reduction

Although the two epochs of observations were conducted consistently in almost every respect, the difference in the telescope position angle can introduce subtle systematic errors in the cross-epoch flux calibration. These errors come from three sources: contamination from the primary VHS 1256 AB; contamination from background sources; and detector systematics. Among these, the difference in the primary star's contaminating flux is the most significant error source and can be mitigated by subtracting the primary PSF consistently.

In Bowler et al. (2020), the light curves of VHS 1256 b were extracted without primary subtraction. This decision was made based on the fact that the contaminating flux has a similar intensity as the sky background and primary subtraction did not significantly affect the *relative* variability measurements. However, cross-epoch calibration requires *absolute* photometry and thus primary subtraction becomes necessary. In the Epoch

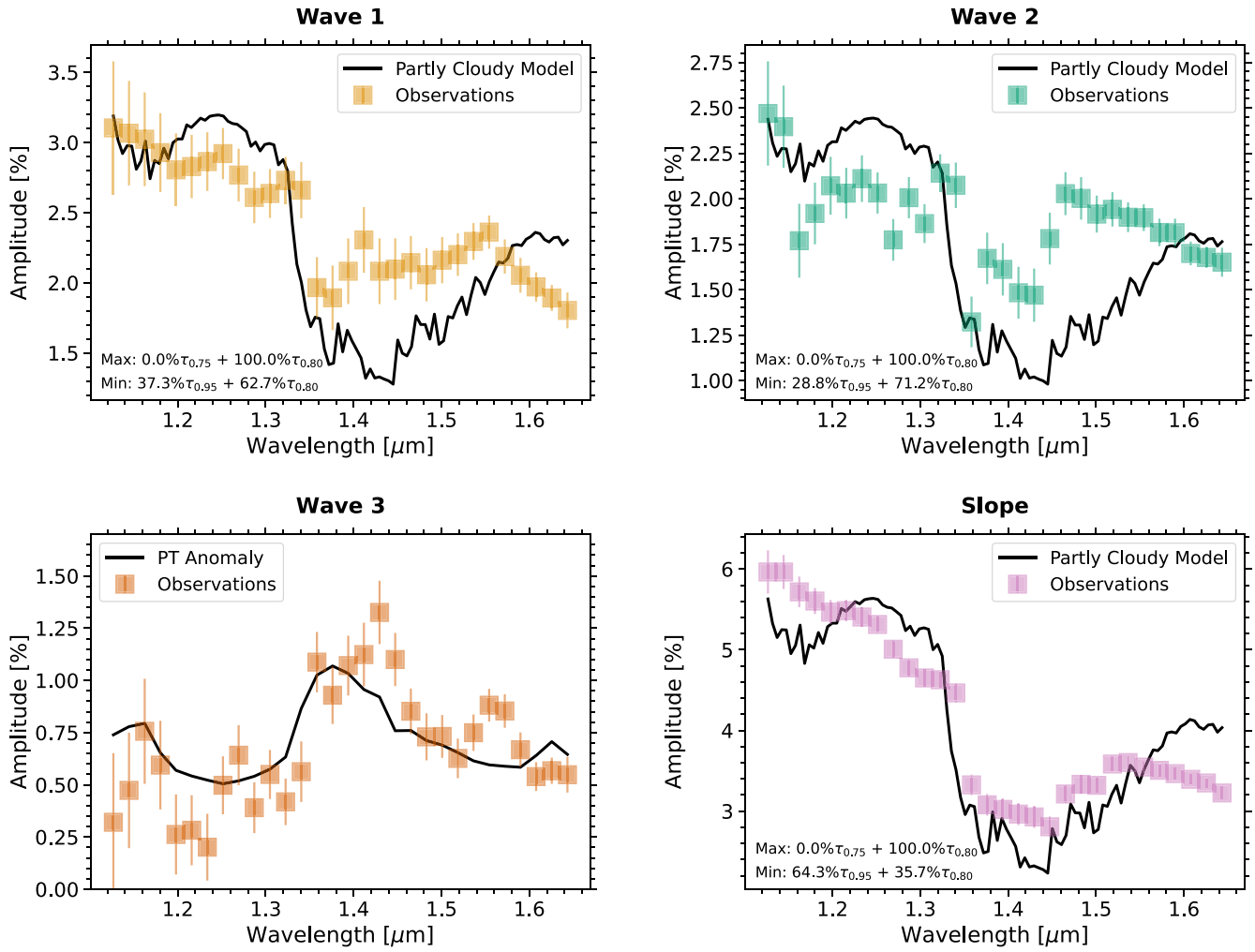

Figure 7. Comparisons of the observed wavelength-dependent amplitudes and atmospheric model predictions. The spectral variability patterns of the sine waves fall into two categories: Wave 1, Wave 2, and the linear trend match well with the prediction of a partly cloudy model; Wave 3 is better fit with a model involving thermal profile anomalies.

2018 observations, the primary binary's PSF contributes 7.8% of the flux relative to the average spectrum of VHS 1256 b in a $R = 4$ pixels extraction window. Without primary subtraction, the contamination would cause biases in measuring the absolute flux. Therefore, instead of directly adopting the results of Bowler et al. (2020), we re-reduced the Epoch 2018 data with the "flip-and-subtraction" method (described in Section 2) and extracted VHS 1256 b's spectra from the primary-subtracted spectral images.

Figure 8 shows the consistently reduced light curves of Epoch 2018 and Epoch 2020. These light curves are not phase-folded, because the current rotational period constraint does not permit precise phase propagation for nearly 900 rotation periods.[11] The flux changes are measured relative to the lowest flux point, which occurred at the beginning of Epoch 2018.

VHS 1256 b is brighter in Epoch 2020 than Epoch 2018 by $16.9\% \pm 1.0\%$ in the time-averaged G141 broadband flux. Relative to the median flux, the broadband peak-to-peak flux difference is $33.3\% \pm 0.2\%$. In the three medium filter bands, the peak-to-peak flux differences decrease slightly with the wavelength: $37.6\% \pm 0.5\%$ in F127M, $37.1\% \pm 1.0\%$ in F139M, and $33.9\% \pm 0.5\%$ in F153M. We note that the quoted errors only include those directly derived from photometry: photon noise, sky background, dark current, and flat field uncertainties. In the next subsection, we discuss additional systematic uncertainties in cross-epoch flux calibration.

4.2. Systematic Uncertainties in Cross-epoch Flux Calibration

Apart from the error due to primary contamination, there are two additional sources of systematic uncertainty that can interfere with cross-epoch flux calibration. The first one is contamination from unknown background sources. As shown in Figure 9, several faint spectral traces are present in the median-combined images. Because of the telescope PA difference between the 2018 and 2020 observations, one faint background spectrum may contaminate VHS 1256 b in one epoch but not the other.

To estimate the contribution of faint contaminating flux to the flux calibration of VHS 1256 b, we visually selected background spectral traces (marked by blue rectangles in Figure 9) and calculated their average contaminating flux in the extraction window ($R = 4$ pixels). Among all sources, the average flux is $0.31 e^- s^{-1}$ column^{-1}, corresponding to 1.4% of VHS 1256 b's average flux in the G141 broad band or 2.2% of the average flux in the water absorption band. These values are

[11] Linearly scaling the uncertainty of the Spitzer light curve period by 900 yields 20 hr, the same order as the rotation period itself.

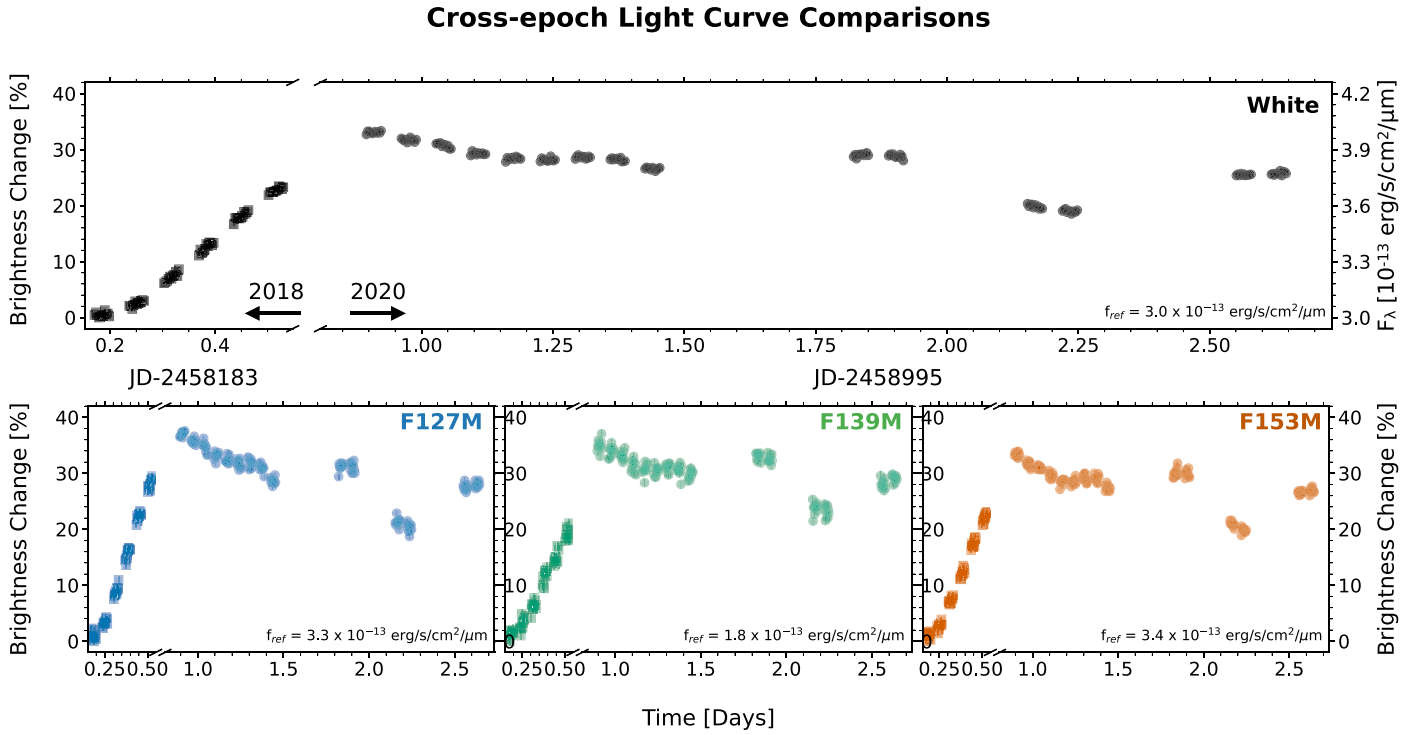

Figure 8. Combined light curves of VHS 1256 b in the 2018 and 2020 epochs. In four representative bands: G141 broad band (top panel), F127M (centered at 1.27 μm, sampling the continuum on the blue side of the water band; bottom left panel), F139M (centered at 1.39 μm, sampling the water band; bottom middle panel), and F153M (centered at 1.53 μm, sampling the continuum on the red side of the water band; bottom right panel). The Epoch 2018 light curves are plotted as squares, and the Epoch 2020 light curves are shown as circles. The light curves are normalized by the minimum flux measured in each band. The reference flux values are indicated at the bottom right corners. The right axis of the top panel marks the broadband flux density in erg s^{-1} cm^{-2} μm^{-1}. The x-axes are broken to fit the two epochs of data.

(The data used to create this figure are available.)

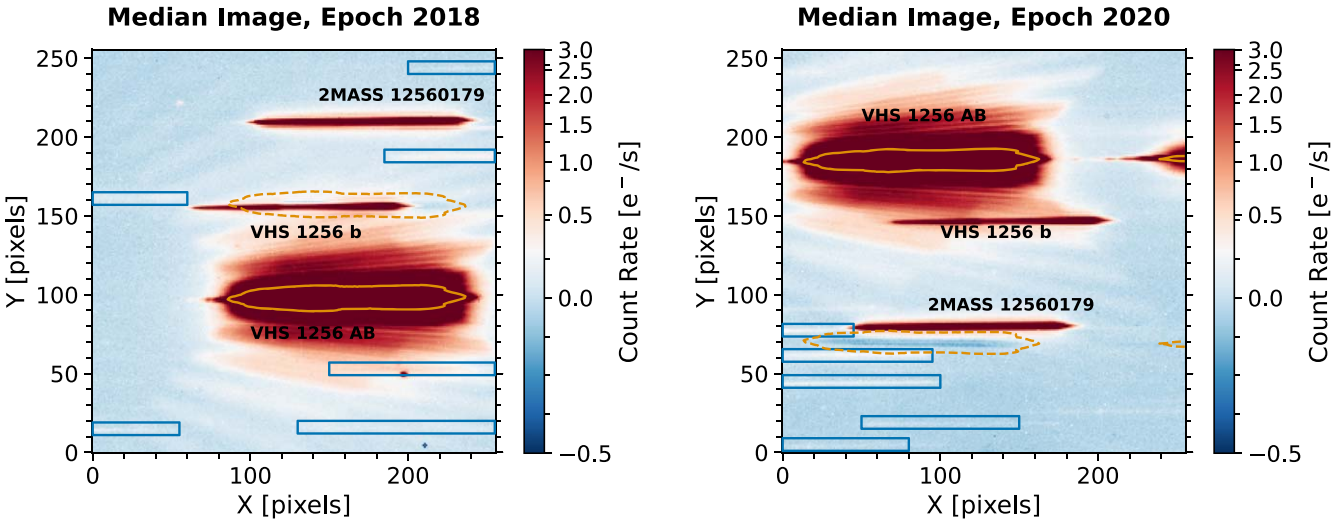

Figure 9. Heavily stretched grism images of VHS 1256 b showing the contaminating sources in the Epoch 2018 (left) and Epoch 2020 (right) observations. The orange solid contours mark a flux level at 1% of the image maximum, highlighting the position of VHS 1256 AB. The primary binary's extended PSF is the major contaminating source in the flux measurements of VHS 1256 b. The orange dashed contours show the position of the cross talk systematics caused by the intense illumination from VHS 1256 AB. The cross talk signal is at a symmetric location relative to the PSF of VHS 1256 AB with respect to the x-axis and has a negative flux. The blue rectangles mark the positions of spectral traces of faint background sources.

likely upper bounds, because no background sources are identified near or overlapping with VHS 1256 b. Only in the unlucky scenario where one background source occupies the exact same pixels as VHS 1256 b can contamination reach these levels.

The second uncertainty source is detector systematics. The flat field uncertainty of WFC3/IR is about 1% per pixel. In the broadband measurements that involve more than 400 pixels, the flat field errors are attenuated to below the 0.1% levels, and thus are unlikely to affect our results. However, one rarely discussed WFC3/IR systematic, cross talk, may have a more significant effect in cross-epoch flux calibration. Cross talk is manifested as a low-level negative and mirrored image of a bright source on the detector. The negative image is at a

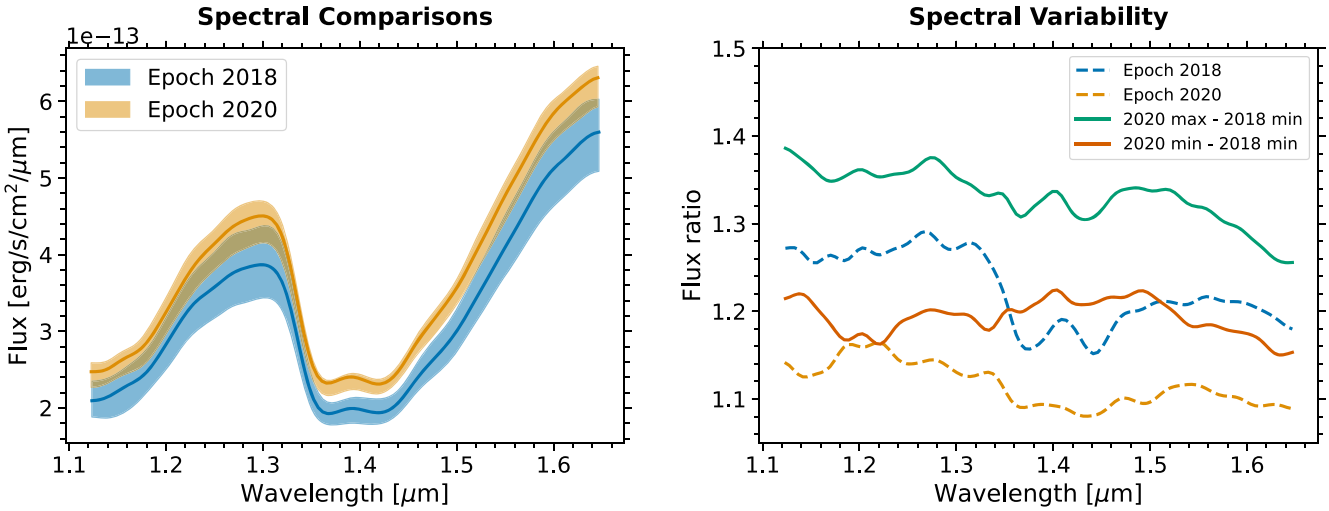

Figure 10. Wavelength-dependent flux variations between Epoch 2018 and Epoch 2020. Left: spectra of VHS 1256 b in Epoch 2018 (blue) and Epoch 2020 (yellow). The solid lines are for the median spectra, and the dashed lines are for the extrema spectra. The shaded regions show the range of spectral variability. Right: representative spectral variability curves. The solid lines show the $F_{\rm max}/F_{\rm min}$ flux ratios between the Epoch 2020 maximum and the Epoch 2018 minimum (green), as well as between the Epoch 2020 minimum and the Epoch 2018 minimum (red). For reference, flux ratio curves derived using the extrema of the same epochs are shown in dashed lines (blue for Epoch 2018; yellow for Epoch 2020).

mirrored position with respect to the x-axis relative to the positive image. In the Epoch 2018 observations, the cross talk image of VHS 1256 AB happened to partially overlap with the spectral trace of VHS 1256 b, possibly reducing the observed flux. To our knowledge, there is no available software to correct for this effect.

To estimate the uncertainty due to cross talk, we locate the negative image in the Epoch 2020 data by mirroring the coordinates of the positive image and calculating the contaminating flux in the extraction window. The average cross talk count rate is -0.37, $e^- s^{-1}$ column^{-1}, corresponding to 1.6% of VHS 1256 b's average G141 broadband flux or 2.5% of its average water band flux.

Combining the two sources of uncertainty in quadrature, we find that the systematic uncertainty in cross-epoch flux calibration is $-0.49\,e^- s^{-1}$ column^{-1}, corresponding to 2.2% of VHS 1256 b's average G141 broadband flux or 3.3% of its average water band flux. The systematic uncertainty is therefore significantly greater than the photometric uncertainty. The uncertainty estimates corroborate what we observed with the background star 2MASS J12560179−1257390, which shares a similar brightness to VHS 1256 b. The background star's light curves are flat in both epochs, but the epoch-averaged flux differ by 1.5% between the two. Based on this analysis, we revise the uncertainties in the cross-epoch flux comparison: $33.3\% \pm 2.2\%$ in the G141 broad band, $37.6\% \pm 2.2\%$ in F127M, $37.1\% \pm 3.4\%$ in F139M, and $33.9\% \pm 1.7\%$ in F153M.

4.3. Cross-epoch Spectral Variability

To further examine cross-epoch spectral variability, we derive the flux ratio between the two epochs (Figure 10). Two cross-epoch comparisons between extrema are presented: the Epoch 2020 maximum versus the Epoch 2018 minimum; and the Epoch 2020 minimum versus the Epoch 2018 minimum. For reference, two same-epoch spectral variability curves are overplotted in Figure 10. As discussed in Bowler et al. (2020) and Zhou et al. (2020) and in previous sections of this paper, both of the two same-epoch curves have lower variability in the 1.40 μm H_2O band than in the continuum, supporting that heterogeneous clouds are the main driver for spectral variability. However, the cross-epoch spectral variability curves differ from the same-epoch curves. The 2020 maximum versus the 2018 minimum flux ratio curve has a gradual trend that decreases from 1.38 at 1.1 μm to 1.25 at 1.65 μm without exhibiting a significant amplitude decrease in the H_2O band. Spectral variability with weak wavelength dependence in the WFC3/G141 bandpass was observed in brown dwarfs (e.g., Yang et al. 2014; Manjavacas et al. 2017; Lew et al. 2020), as well as the planetary-mass object PSO J318.22 that has an identical spectral type to VHS 1256 b (Biller et al. 2018). Models invoking heterogeneous haze layers or modified local temperature gradients have been proposed to reproduce this spectral change (Yang et al. 2014; Tremblin et al. 2020).

5. Discussion

5.1. Interpreting the Periodicity of VHS 1256 b's Light Curves

VHS 1256 b's light curves exhibit multiple periods that differ from each other significantly. These periods include: 22.04 ± 0.05 hr (Spitzer 4.5 μm, Zhou et al. 2020), 18.8 ± 0.2 hr (Wave 1), 15.1 ± 0.2 hr (Wave 2), and 10.6 ± 0.1 hr (Wave 3). Additionally, fitting a single sinusoid to the 9 hr long Epoch 2018 light curve yields a period of 22.5 ± 0.5 hr, similar to the one determined by the Spitzer observations. The periodicity in brown-dwarf light curves is often interpreted as rotation rates (e.g., Metchev et al. 2015; Zhou et al. 2016, 2020). The apparently incompatible measurements demonstrate the challenges in precisely determining the rotation periods using light curves. We discuss the origins of discrepancies between these periods and the implications on rotation measurements.

The circulation patterns probed by a finite-length light curve are incomplete. When estimating the rotation periods with light curve fitting, unaccounted model complexity can lead to biased results. For example, if the true light curve during the Spitzer observation is our best-fitting three waves but modeled (inaccurately) by a single sinusoid, the probability of

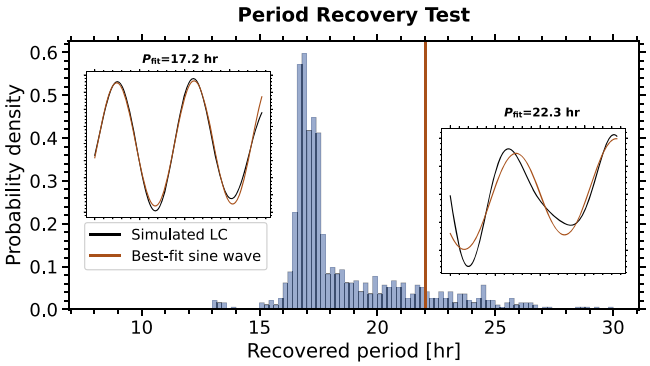

Figure 11. Distribution of the best-fitting periods of a 36 hr light curve segment obtained from a period-recovery test. In this test, a single sine wave is fit to 10,000 random 36 hr segments of VHS 1256 b's evolving light curve, which is assumed to be the multiple-sinusoidal model that we found in the Epoch 2020 data. We show the results with a histogram that is normalized so that an integral of the probability density equals to 1. The distribution peaks at 17 hr, the average period of Waves 1 and 2. It also has a long tail extending toward long periods, suggesting a nonnegligible probability to detect a signal with period $P_{\rm fit} \geqslant 22$ hr. Two embedded panels show examples of light curve segments fit by models with different periods. Based on this result, we can at least partially attribute the apparent discrepancy in period measurements between the HST and Spitzer observations to the limited observing windows.

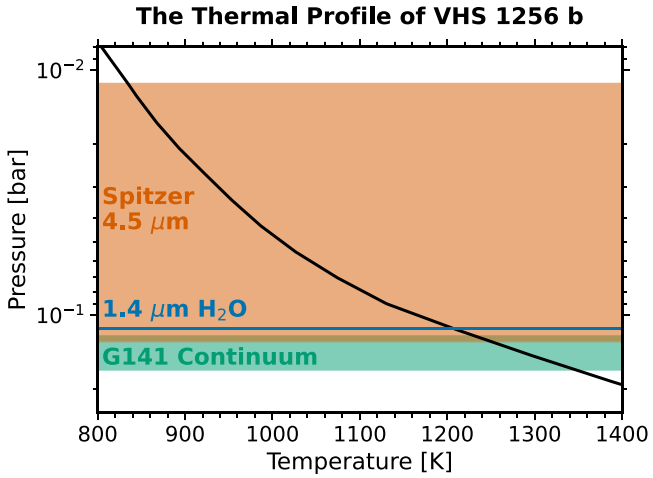

Figure 12. Thermal profile of VHS 1256 b and pressure levels probed by various bandpasses. The black solid line is the *T-P* profile of the best-fitting atmospheric model found by Zhou et al. (2020; $T_{\rm eff} = 1000$ K, $\log g = 3.2$, $f_{\rm sed} = 1.0$, 80% cloud optical depth of the fully cloudy model). The green, blue, and orange horizontal bands/lines mark the pressure levels probed by the WFC3/G141 continuum ($\lambda < 1.30\ \mu$m or $\lambda > 1.50\ \mu$m), the 1.4 μm H_2O band, and the Spitzer 4.5 μm channel, respectively. These pressure levels are mapped from the observed brightness temperatures based on the thermal profile. The lower pressure levels probed by the Spitzer band compared to those by WFC3/G141 may contribute to the difference in period measurements between the two bands.

recovering a period of $P \geqslant 22$ hr is considerable (Figure 11). Likewise, substantial systematic uncertainties can occur in fitting the HST light curves with the multiple-sinusoidal models. If we replace the linear trend, which is essentially a first-order approximation of an unknown long-term variation, with a long-period ($42\ {\rm hr} < P < 210\ {\rm hr}$) sinusoid, the best-fitting periods of the three waves can vary by ~1 hr (5%–10% relative errors), driving the period of Wave 1 closer to the Spitzer period in several cases. These results show that the systematic uncertainties caused by fitting an incomplete model can considerably exceed the least-squares-determined uncertainty when insufficient monitoring does not reveal the light curve's underlying evolving patterns.

Differential rotation and atmospheric circulation further complicate period measurements. GCM simulations in Showman et al. (2019) exhibit significant time-variable vertical shear in the zonal wind. As shown in Figure 12, the pressure levels probed by the WFC3/G141 observations are deeper than those probed by the Spitzer 4.5 μm channel. A vertical wind shear in VHS 1256 b could lead to different period measurements between these two bands. Furthermore, GCMs in Showman et al. (2019) and Tan & Showman (2021b) predicted quasiperiodic velocity and directional changes in the zonal waves. Using periodograms of the GCM-simulated light curves, Tan & Showman (2021b) showed that the zonal waves could shift and broaden the power spectrum peaks near the underlying rotation periods. As a result, light curve periodicity indeed probes the rotation rate, but imprecisely. In the same periodogram, secondary peaks of zonal wavenumber $k = 2$ are a common structure.

Assuming that the best-fitting sine waves probe atmospheric structures (e.g., planetary-scale waves and jets; See Section 5.2), the shorter periods of Waves 1 and 2 relative to the Spitzer period suggest that they trace eastward-propagating structures, and the period of Wave 3 is consistent with a $k = 2$ harmonic. We convert periods to equatorial spin velocities by assuming $R = 1.17\ R_{\rm Jup}$ (Dupuy et al. 2020) and find that Waves 1 and 2 travel at 1.1 km s^{-1} and 3.0 km s^{-1}, respectively. These results are at best order-of-magnitude estimates and are likely dominated by the observing-window-related systematics. Continuous and long-term time-resolved observations (e.g., Apai et al. 2017, 2021) will allow for more accurate period measurements and wind speed constraints.

5.2. Atmospheric Circulation in VHS 1256 b

The markedly evolving light curves indicate vigorous atmospheric dynamical processes in VHS 1256 b. The underlying circulation patterns can be probed through top-of-the-atmosphere mapping that translates light curves into two-dimensional structures (e.g., Crossfield et al. 2014; Karalidi et al. 2015; Plummer & Wang 2022). However, because our data are scarcely sampled and have a limited time baseline, the mapping results are highly degenerate. In this subsection, we construct simplified mapping models that are plausible for VHS 1256 b based on recent theoretical work (e.g., Zhang & Showman 2014; Showman et al. 2019; Tan & Showman 2021b) and compare these models with the observed light curves.

Using GCMs that couple atmospheric dynamics with cloud formation and its radiative effect, Tan & Showman (2021b) identified two types of structures that cause light curves to evolve: zonal waves and vortices. Waves propagate zonally at various velocities, and their changing phase differences result in emerging flux variability. Vortices are zonally stationary and impact the light curves by their stochastic transformations accompanied by cloud formation, dissipation, and thermal profile perturbation. Waves often have a stronger effect in the light curves, particularly in fast-rotating models ($P_{\rm rot} \leqslant 10$ hr) that are viewed equator-on (Tan & Showman 2021b). However, vortex variability is traceable in synthetic light curves of slow-rotating models ($P_{\rm rot} < 10$ hr), because the vortex size increases linearly with the rotation period, and long periods allow vortices to evolve sufficiently in one rotation. VHS 1256 b is a slow rotator, so both waves and vortices should be considered. Therefore, we adopt an agnostic approach and experiment with various combinations of waves

and vortices. Our mapping models can be grouped into three scenarios: (a) wave-dominated; (b) spot-dominated; (c) a mixture of wave and spots.

We briefly summarize the modeling approach here and provide details in the Appendix. Zonal waves are modeled as sinusoids with periods being free parameters to allow for the possibility of high-wavenumber components and differential rotation. Vortices are modeled as circular spots characterized by their sizes, positions, and contrasts. To reduce degeneracy and enable meaningful comparisons between the data and the model, we place the following restrictions on spot properties:

1. The angular size of any spot is fixed to 15°, a limit determined by the Rossby deformation radius ($R_{\rm spot} \approx 0.25R_{\rm Jup}$; Equation (A2)). Notably, because the spot size is a small fraction (<10%) of a hemisphere, the light curve of a dark/bright spot transit appears like an eclipse/bump rather than a sinusoid.
2. The spots are longitudinally stationary and corotate with the sphere at a period of $P_{\rm rot} = 22.0$ hr. Their latitudes are fixed to 45° to reflect the fact that vortices are populated at mid-to-high latitudes (Tan & Showman 2021b).
3. The spot has a uniform brightness contrast that can linearly vary with time, but the sign of the contrast cannot change (i.e., a dark spot cannot become a bright one and vice versa).

With these constraints, a spot is modeled by three parameters: longitude, average contrast, and contrast variability. The three model types are constructed by linearly combining sinusoids and spot light curves.

5.2.1. Scenario 1: Wave-dominated Mapping

Assuming the light curve evolution is dominated by zonal waves, we can map the sinusoids in the three-sine-wave model (Section 3.1) into three atmospheric waves. This is similar to the planetary-scale wave mapping that explained long-term ($>100P_{\rm rot}$) photometric evolution in several brown dwarfs (Apai et al. 2017, 2021). Assuming the true rotation period is the 22.0 hr period measured by Spitzer (Zhou et al. 2020), the 18.6 and 15.1 hr sinusoids (Waves 1 and 2) are two eastward traveling waves in which cloud thickness modulates in a wavenumber $k = 1$ pattern and the 10.5 hr sinusoid corresponds (Wave 3) to thermal profile modulation in a $k = 2$ pattern. Differential propagation of the three waves can explain most of the photometric and spectroscopic variability observed in Epoch 2020 except for the linear trend. A polar spot in which cloud dissipates in combination with a slightly tilted spin-axis that allows the polar region to be constantly visible is a possible explanation.

5.2.2. Scenario 2: Spot-dominated Mapping

We can also begin with the assumption that the observed light curve evolution is the consequence of vortex transformation and construct a light curve model that only contains time-varying circular spots and a long-term linear trend. We fit this model to the Epoch 2020 light curve with an incremental increase in the number of spots. We find that a reasonable fit requires at least three spots ($\chi^2 = 613$, DOF = 154, in comparison to $\chi^2 = 346$, DOF = 154 for the three-sine-wave model). The left panel of Figure 13 shows a possible solution consisting of a dimming bright spot and a pair of bright and dark spots locating at the opposite longitudes. Fitting to the light curve requires the latter spot pairs to change contrasts in divergent directions. All three spots have significant contrast variations between the two periods. The contrasts of the two bright spots change by 25% and 50%, corresponding to brightness temperature variations ($\Delta T_{\rm B}$) of 60 K and 110 K, respectively. Variability introduced by the dark spot (8%–18%) exceeds the maximum for a $R = 15°$ spot (~6.6% for a nonemitting spot), suggesting that a size much greater than the Rossby deformation radius or multiple coevolving dark spots are required for this solution to be physically plausible. When the sign of spot contrast is allowed to change, a two-spot model can fit the light curve, albeit an even more rapid contrast variation is needed (Figure A4).

5.2.3. Scenario 3: A Mixture of Waves and Spots

Finally, we attempt to reproduce the light curve with a mixture of waves and spots. The number of mapping elements is limited to three or fewer to avoid overfitting. The right panel of Figure 13 shows the best-fitting configuration ($\chi^2 = 391$, DOF = 154, in comparison to $\chi^2 = 346$, DOF = 154 for the three-sine-wave model). This model consists of two sinusoids ($P_1 = 20.0 \pm 0.1$ hr, $A_1 = 3.4\% \pm 0.1\%$; $P_2 = 14.9 \pm 0.1$ hr, $A_2 = 1.5\% \pm 0.1\%$) and a bright spot with a nearly constant contrast (60% brighter or $\Delta T_{\rm B} = 125$ K higher than the background). The solution is not unique and alternative model configurations (e.g., one sinusoid and two spots) can fit the light curve reasonably well (see examples in the Appendix).

5.2.4. Model Interpretation and Future Perspectives

Models that fit the light curve well all contain features that are not fully consistent with atmospheric dynamical models. For example, the wave-dominated mapping requires differential rotation of high velocity ($v \sim 2\ {\rm km\ s^{-1}}$) that exceeds the maximum wind speed in the GCMs of Tan & Showman (2021b). In the vortex-dominated case, the rapid and seemingly coordinated variations of two spots in the opposite longitudinal positions are also improbable. Increasing the model flexibility by adding more spots or allowing the spot size to vary with time may reconcile these incompatibilities, although these more complex models are not warranted by our data. Meanwhile, the extremely high amplitude variability seen in VHS 1256 b poses a challenge to state-of-the-art GCMs that do not produce variability of more than a few percent. More realistic cloud and radiative transfer modeling could result in a better match between GCMs and the observed results.

Although we purposely restrict our models to several simplified cases, we still find a variety of maps that can reproduce VHS 1256 b's light curve (Appendix). The high degeneracy underscores the limitation of short and sparsely sampled observations in probing circulation patterns. Long-term and contiguous light curves can distinguish the origin of light curve evolution, because the difference between wave beating and stochastic vortex variability becomes unambiguous when the time baseline is beyond one or two rotation periods. For all published long-term (>30 rotations) brown-dwarf light curves (2M1324, $P_{\rm rot} = 13.2$ hr; 2M2139, $P_{\rm rot} = 8.2$ hr; and SIMP0136, $P_{\rm rot} = 2.4$ hr in Apai et al. 2017 and Luhman16 AB, $P_{\rm rot} = 5.3$ hr[12] in Apai et al. 2021), zonal-wave-dominated

[12] This is the period of Luhman16 B that shows a higher amplitude in the binary.

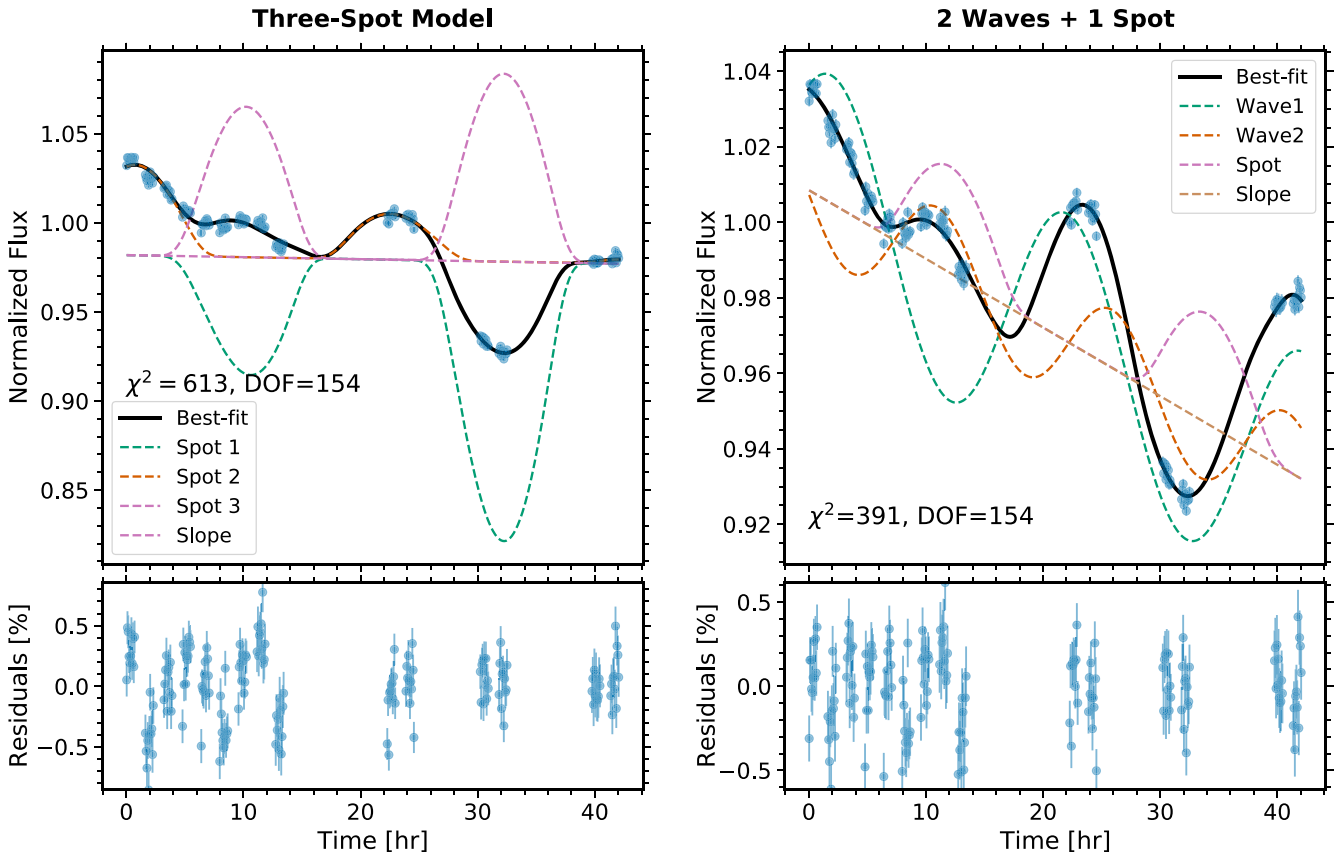

Figure 13. Alternative decompositions of the broadband light curves. Left: a model composed of three variable spots; right: a model composed of two waves and a variable bright spot. The solid lines, representing the best-fitting models, fit the data reasonably well. The dashed lines show individual model components. The fitting solutions are not unique due to parameter degeneracy. We show additional examples in the Appendix.

maps with occasional additions of spots are the only model that has been shown to agree with the observations. Whether VHS 1256 b, a slower rotator, has similar atmospheric dynamical properties requires further investigation. Doppler imaging (Crossfield et al. 2014) and time-resolved polarization observations (e.g., Millar-Blanchaer et al. 2020; Mukherjee et al. 2021) can also offer unique constraints on the circulation patterns of VHS 1256 b.

5.3. The Extremely High Amplitude Variability of VHS 1256 b

The brightness change observed in VHS 1256 b is the highest found in brown dwarfs. The 33% peak-to-peak flux variation observed in VHS 1256 b exceeds the previous largest brown-dwarf variability amplitude observed in the *J*-band light curve of 2MASS J21392676+0220226 (Radigan et al. 2012; Apai et al. 2013) In Zhou et al. (2020), we have shown that the asynchronously observed spectral variability in the HST/WFC3/G141 band and the Spitzer 4.5 μm channel could be very well explained by cloud optical depth changes. In this work, we further demonstrate that thermal profile anomalies in addition to heterogeneous clouds may contribute to observed spectral variability.

VHS 1256 b has several properties that are favorable for producing high amplitude variability. It is likely young and has a low surface gravity (Dupuy et al. 2020), resulting in a large atmospheric scale height and geometrically thick clouds. The latter is also evident from its unusually red infrared colors (Gauza et al. 2015; Rich et al. 2016). These conditions permit significant spatial variations in the cloud optical depth that leads to high amplitude rotational modulations. VHS 1256 b has an edge-on viewing geometry that maximizes the effect of heterogeneous atmospheric structures on photometric and spectral variability (Vos et al. 2017). Results from Tan & Showman (2021a, 2021b) also show that the relatively slow rotation rate of VHS 1256 b may also indirectly contribute to its high variability, because slow rotators are likely to have thicker clouds, larger-sized vortices and therefore larger temporal flux changes.

Brown dwarfs and planetary-mass objects that share almost identical near-infrared spectra to VHS 1256 b, such as PSO J318.5-22 (Biller et al. 2015) and WISEP J004701 +680352 (Lew et al. 2016), also exhibit high amplitude variability. Directly imaged exoplanets with similarly red near-infrared colors (e.g., HR 8799bcde Marois et al. 2008, 2010, HD 95086b Rameau et al. 2013; De Rosa et al. 2016) are candidates for detecting variable brightness and spectra. Based on the complexity of the heterogeneous structures in VHS 1256 b we have found in this work, monitoring programs for these planets (e.g., Apai et al. 2016; Biller et al. 2021; Wang et al. 2022) will provide a better understanding of how these physical properties play a role in the observed rotational variability.

6. Summary

We analyzed HST/WFC3 time-resolved spectra of the L7-type planetary-mass companion VHS 1256 b and found high amplitude and wavelength-dependent variability. The evolving spectra reveal heterogeneous distributions of clouds and thermal profiles in the atmosphere of the companion and

enable an investigation of the atmospheric dynamical processes that shape these structures. We list our findings as follows:

1. In a new HST time-resolved observing campaign, VHS 1256 b was spectroscopically monitored by WFC3/G141 with a time baseline of 42 hr (approximately two rotation periods). The brown-dwarf companion exhibited significant variability in its spectrum and light curve between the two rotation periods.
2. VHS 1256 b's fast-evolving light curves are more complex than previously reported. A combination of three sine waves in which the periods are free parameters fits the light curve well. For the 1.12 to 1.65 μm broadband light curve, the best-fitting sine-wave periods are 18.8 ± 0.2 hr, 15.1 ± 0.2 hr, and 10.6 ± 0.1 hr, and the corresponding peak-to-peak amplitudes are $5.8\% \pm 0.8\%$, $4.6\% \pm 0.7\%$, and $1.4\% \pm 0.1\%$. A linear trend is a necessary component of the light curve model to explain the long-term light curve variation.
3. VHS 1256 b exhibits clear spectral variability in the new epoch. The difference between the maximum and minimum brightness spectra decreases in the 1.4 μm band, which is qualitatively consistent with its behavior in a previous HST observing epoch (Bowler et al. 2020; Zhou et al. 2020).
4. We fit the three-sine-wave model to spectroscopically resolved light curves to quantify the spectral variability. We find that the amplitudes of all three waves and the linear trend are wavelength dependent. The two long-period waves and the linear trend have a higher amplitude in the continuum than in the H_2O band, resembling the spectral variability caused by clouds with heterogeneous optical depths. In contrast, the shortest period wave has a higher amplitude in the water band than in the continuum, resembling the spectral variability caused by perturbations to the thermal profile.
5. By consistently reducing two epochs of HST/WFC3 observations of VHS 1256 b, we estimate VHS 1256 b's variability on a timescale of nearly 900 rotation periods and find that the variability amplitude between the two epoch is greater than those within individual epochs. The peak-to-peak flux difference is $33.3\% \pm 2.2\%$ in the G141 broad band and reaches to $37.6\% \pm 2.2\%$ at 1.27 μm. These brightness changes are among the strongest ever found in brown dwarfs.
6. The spectral change between the two epochs has a weak wavelength dependence. The decrease in the variability amplitude in the 1.4 μm band detected in individual epochs is absent in the cross-epoch measurement. This suggests that the observed long-term variability and rotational modulations are caused by different atmospheric structures.
7. The rapidly evolving light curves can be reproduced by a variety of physically plausible models that are constructed based on zonal waves, spots, or a mixture of waves and spots. Long-term and continuous light curves can help pinpoint the circulation regime of VHS 1256 b.
8. Uncertainties in the true underlying light curve model can impair the degree to which we can estimate VHS 1256 b's rotation period. Atmospheric evolution can bias the period results by 5%–10%, far exceeding the least-squares-determined uncertainties. Reducing these systematic uncertainties also requires extending the observing time baseline.

Our work has two broad implications that should be considered in future studies. First, the strong variability of VHS 1256 b, an excellent analog to giant exoplanets such as HR8799 bcde, further proves that atmospheric dynamics fundamentally shapes the spectral appearance of planetary atmosphere, and that understanding the 3D atmospheric dynamics is critical for interpreting time-series observations. Second, long-term spectroscopic monitoring observations deliver a wealth of information. Expanding such observing programs to more targets and broader wavelength ranges (e.g., with JWST) will provide valuable data that will help probe atmospheric dynamics in planets and brown dwarfs.

We thank the anonymous referees for detailed and constructive reports. We thank Dr. Xianyu Tan for a helpful discussion about atmospheric dynamical modeling. Y.Z. acknowledges support from the Harlan J. Smith McDonald Observatory Fellowship and the Heising-Simons Foundation 51 Pegasi b Fellowship. B.P.B. acknowledges support from the National Science Foundation grant AST-1909209, NASA Exoplanet Research Program grant 20-XRP20_2-0119, and the Alfred P. Sloan Foundation. C.V.M. acknowledges support from the National Science Foundation grant AST-1910969. This research has made use of the NASA Exoplanet Archive, which is operated by the California Institute of Technology, under contract with the National Aeronautics and Space Administration under the Exoplanet Exploration Program. The observations and data analysis works were supported by program HST-GO-16036. Support for program number HST-GO-16036 was provided by NASA through a grant from the Space Telescope Science Institute, which is operated by the Association of Universities for Research in Astronomy, Incorporated, under NASA contract NAS5-26555.

Facility: Hubble Space Telescope.

Software: `Numpy` (Harris et al. 2020), `Scipy` (Virtanen et al. 2020), `Matplotlib` (Hunter 2007), `Seaborn` (Waskom 2021), `Astropy` (Robitaille et al. 2013), `Pysynphot` (STScI Development Team 2013), `Lmfit` (Newville et al. 2014), `emcee` (Foreman-Mackey et al. 2013), `Starry` (Luger et al. 2019).

Appendix
Decomposing the Epoch 2020 Light Curve

A.1. The Modeling Approach

To explore the circulation patterns in VHS 1256 b, we decompose its Epoch 2020 broadband light curve into sinusoids (zonal waves) and circular spots (vortices). The light curve model is akin to the multisinusoidal model (Equation (1)) with inclusions of spot components. An N sinusoids and M spots model is expressed as:

$$F(t) = C_0 + C_1 t + \sum_{i=1}^{N} \sin(P_i, A_i, B_i) + \sum_{j=1}^{M} \mathrm{spot}(l, \theta, V). \tag{A1}$$

l, θ, and V are the longitude, brightness contrast, and linear contrast variability of a spot. One sinusoid or one spot adds three free parameters, so the total number of free parameter is $2 + 3 * (N + M)$. We restrict model complexity by $N + M \leqslant 3$.

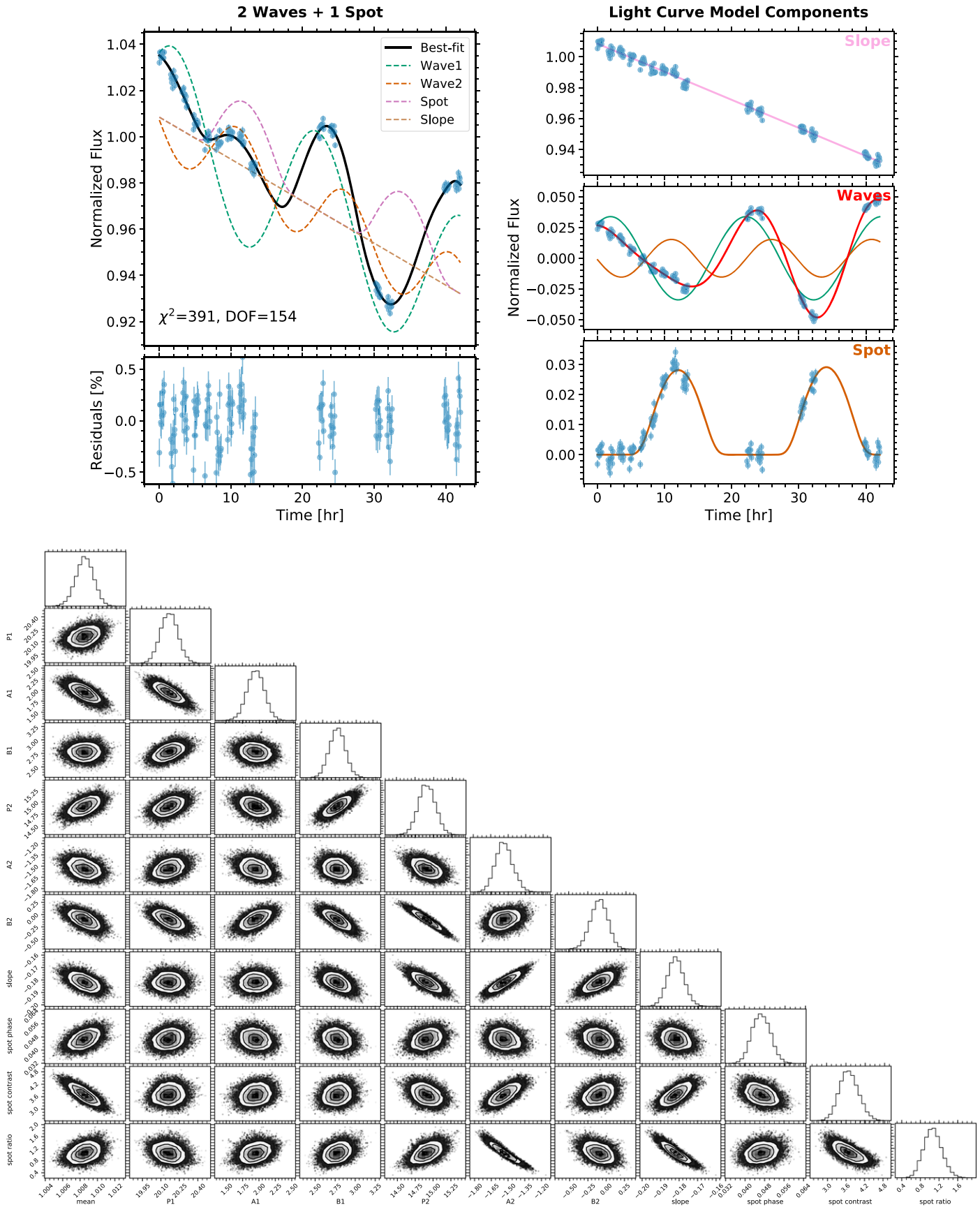

Figure A1. Two waves + one spot light curve decomposition.

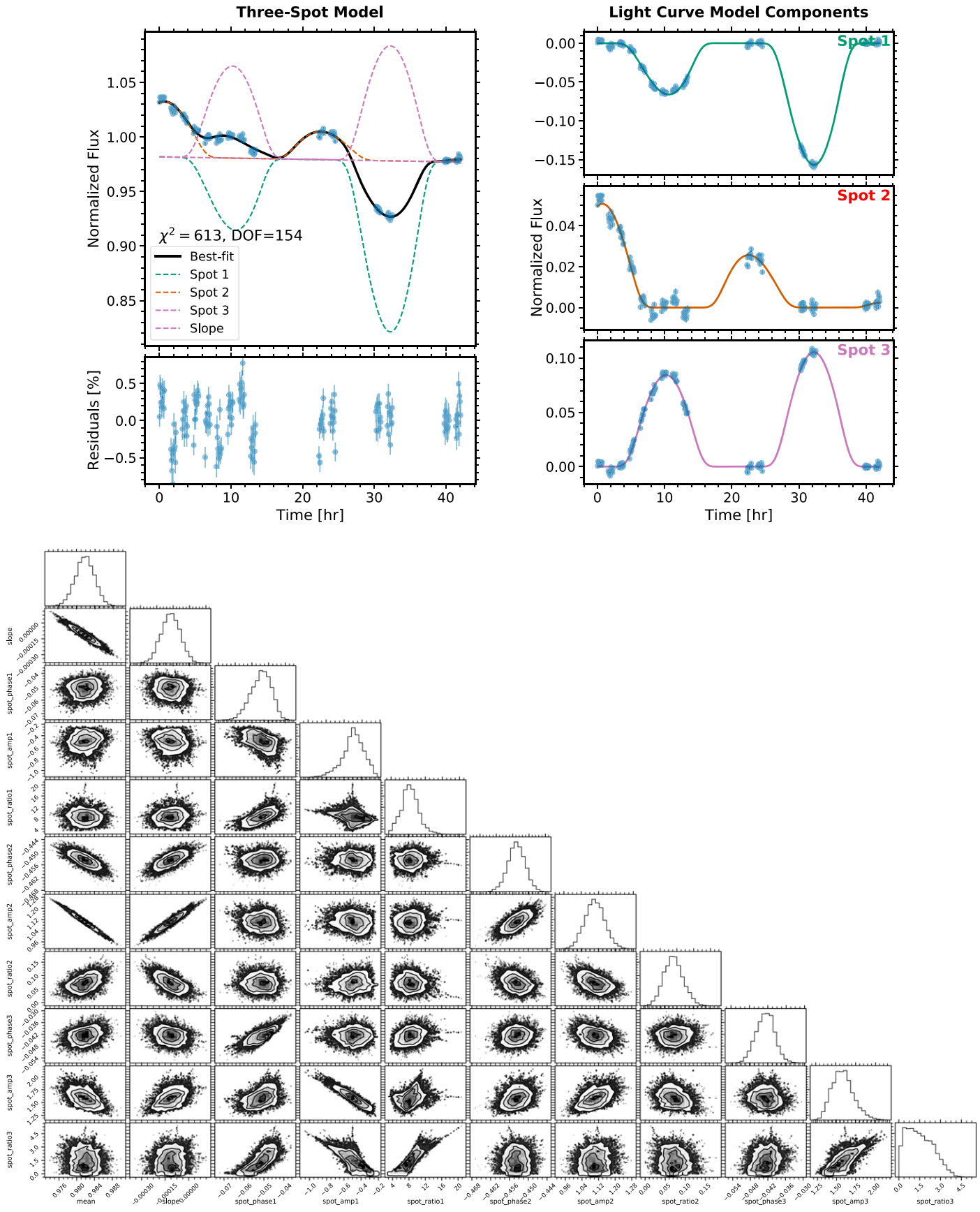

Figure A2. Three-spot light curve decomposition.

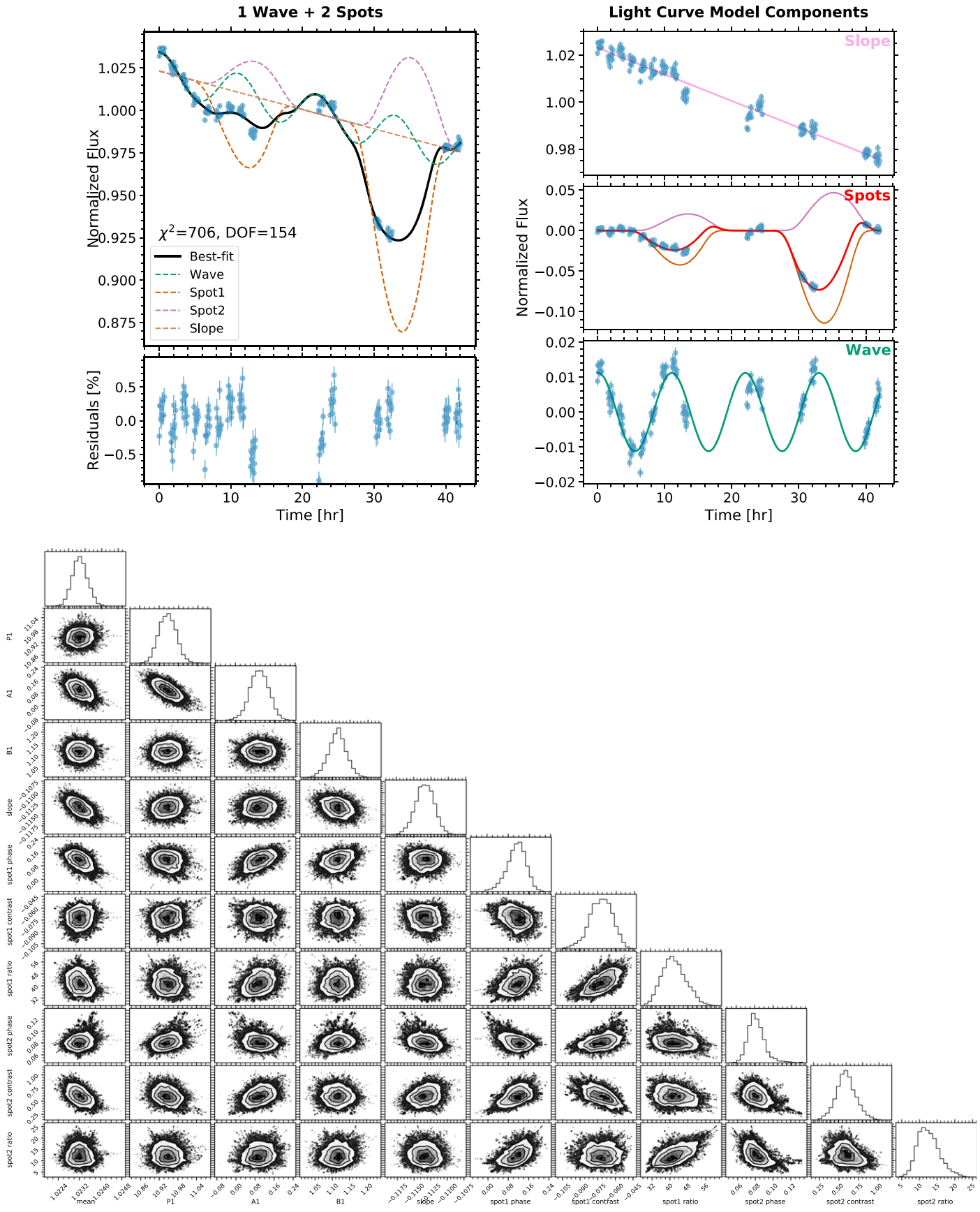

Figure A3. One wave ($k = 2$) + two spots light curve decomposition.

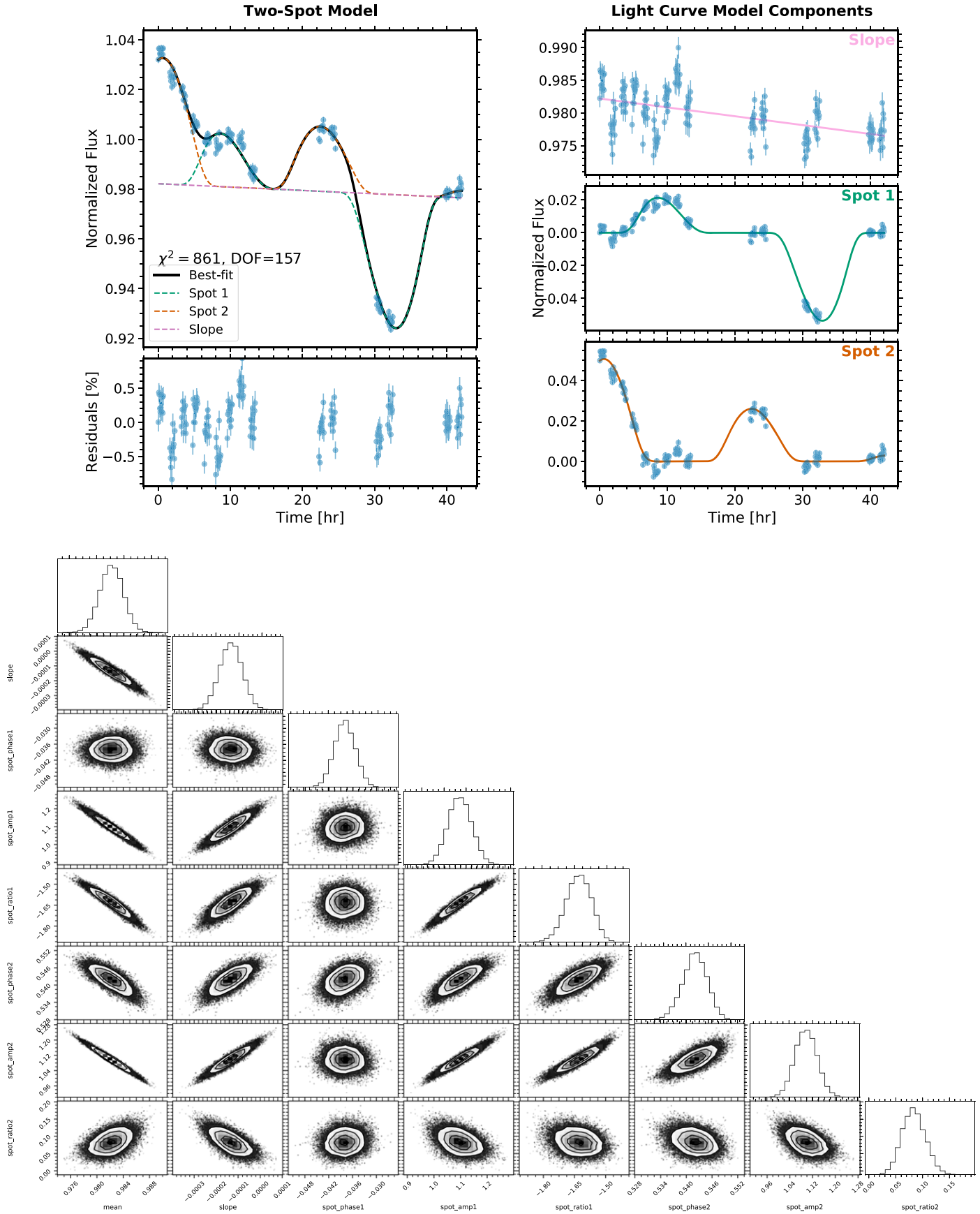

Figure A4. Two-spot light curve decomposition.

The spot light curve is precalculated using `starry` (Luger et al. 2019) with $R_{\rm spot} = 15°$, $\rm lat_{spot} = 45°$, and a contrast ratio of 2 (i.e., the spot is 100% brighter than the global average, corresponding to $\Delta T_{\rm B} = 189$ K in a $T_{\rm B} = 1000$ K sphere). The spot size is assumed to be the Rossby deformation radius, which is the typical size of a vortex driven by cloud radiative feedback (Tan & Showman 2021b)

$$R_{\rm Rossby} = \frac{c_g}{2\Omega \sin\phi} = 0.25 R_{\rm Jup} * \left(\frac{c_g}{2000\ {\rm m\ s^{-1}}}\right)\left(\frac{T}{22\ {\rm hr}}\right)\left(\frac{\sin\phi}{\sin(\pi/4)}\right)^{-1}, \quad \text{(A2)}$$

in which c_g is the gravity wave phase speed, Ω is the rotation rate, and ϕ is the spot latitude. Given a set of l, θ, and V, the spot light curve is phase shifted by l and multiplied by a linear amplitude term $\theta + Vt$. In all but one cases (Figure A4), θ and V are restricted a priori to preclude a sign change in $\theta + Vt$ during our 42 hr observing window.

We optimize the free parameters by first a least-squares fitting using `LMFIT` and then an MCMC. The likelihood function and posterior probability are derived in the same way as the multisinusoidal model fit. In each case, the χ^2 value is recorded to evaluate the fitting quality. Among all experiments with $N + M \leqslant 3$, the three-sine-wave model has the lowest χ^2. Nevertheless, relaxing the restrictions and then fine-tuning the spot properties may result in even better fits.

For each set of N and M, multiple solutions that corresponds to a local χ^2 minimum may exist. We do not attempt to exhaust all possible solutions, but only use these experiments to demonstrate the fact that our current data are not yet able to pinpoint the circulation patterns in VHS 1256 b.

A.2. Examples of Light Curve Decomposition

Figures A1–A4 illustrate a few examples of light curve decomposition results. These four figures correspond to:

A1, two sinusoids and one bright spot;

A2, one dark spot and two bright spots;

A3, one ($k = 2$) wave, one bright spot, and one dark spot;

A4, two spots. In Figure A4, the spot contrast is allowed to switch sign. The rapid spot evolution enables a good fit with only two spots.

In each figure, the top panel is in the same format as Figure 3, showing the observation-model comparison on the left and highlighting the model components on the right. The bottom panel is a corner plot demonstrating the posterior distributions of the model parameters.

ORCID iDs

Yifan Zhou https://orcid.org/0000-0003-2969-6040
Brendan P. Bowler https://orcid.org/0000-0003-2649-2288
Dániel Apai https://orcid.org/0000-0003-3714-5855
Tiffany Kataria https://orcid.org/0000-0003-3759-9080
Caroline V. Morley https://orcid.org/0000-0002-4404-0456
Marta L. Bryan https://orcid.org/0000-0002-6076-5967
Andrew J. Skemer https://orcid.org/0000-0001-6098-3924
Björn Benneke https://orcid.org/0000-0001-5578-1498

References

Ackerman, A. S., & Marley, M. S. 2001, ApJ, 556, 872
Allers, K. N., Vos, J. M., Biller, B. A., & Williams, P. K. G. 2020, Sci, 368, 169
Apai, D., Karalidi, T., Marley, M. S., et al. 2017, Sci, 357, 683
Apai, D., Kasper, M., Skemer, A., et al. 2016, ApJ, 820, 40
Apai, D., Nardiello, D., & Bedin, L. R. 2021, ApJ, 906, 64
Apai, D., Radigan, J., Buenzli, E., et al. 2013, ApJ, 768, 121
Beichman, C., Benneke, B., Knutson, H., et al. 2014, PASP, 126, 1134
Best, W. M. J., Liu, M. C., Magnier, E. A., & Dupuy, T. J. 2021, AJ, 161, 42
Biller, B. A., Apai, D., Bonnefoy, M., et al. 2021, MNRAS, 503, 743
Biller, B. A., Vos, J., Buenzli, E., et al. 2018, AJ, 155, 95
Biller, B. A., Vos, J. M., Bonavita, M., et al. 2015, ApJL, 813, L23
Artigau, É., Bouchard, S., Doyon, R., & Lafrenière, D. 2009, ApJ, 701, 1534
Bowler, B. P., Liu, M. C., Mawet, D., et al. 2017, AJ, 153, 18
Bowler, B. P., Zhou, Y., Morley, C. V., et al. 2020, ApJL, 893, L30
Buenzli, E., Apai, D., Morley, C. V., et al. 2012, ApJL, 760, L31
Buenzli, E., Apai, D., Radigan, J., Reid, I. N., & Flateau, D. 2014a, ApJ, 782, 77
Buenzli, E., Saumon, D., Marley, M. S., et al. 2014b, ApJ, 798, 127
Burningham, B., Faherty, J. K., Gonzales, E. C., et al. 2021, MNRAS, 506, 1944
Burrows, A. S., Sudarsky, D., & Hubeny, I. 2006, ApJ, 640, 1063
Chabrier, G., Johansen, A., Janson, M., & Rafikov, R. 2014, in Protostars and Planets VI, ed. H. Beuther et al. (Tucson, AZ: Univ. of Arizona Press), 619
Charnay, B., Bézard, B., Baudino, J.-L., et al. 2018, ApJ, 854, 172
Crossfield, I. J. M., Biller, B. A., Schlieder, J. E., et al. 2014, Natur, 505, 654
De Rosa, R. J., Rameau, J., Patience, J., et al. 2016, ApJ, 824, 121
Dupuy, T. J., Liu, M. C., Evans, E. L., et al. 2022, arXiv:2208.08448
Dupuy, T. J., Liu, M. C., Magnier, E. A., et al. 2020, RNAAS, 4, 54
Eriksson, S. C., Janson, M., & Calissendorff, P. 2019, A&A, 629, A145
Faherty, J. K., Riedel, A. R., Cruz, K. L., et al. 2016, ApJS, 225, 10
Foreman-Mackey, D., Hogg, D. W., Lang, D., & Goodman, J. 2013, PASP, 125, 306
Gao, P., Marley, M. S., & Ackerman, A. S. 2018, ApJ, 855, 86
Gauza, B., Béjar, V. J. S., Pérez-Garrido, A., et al. 2015, ApJ, 804, 19
Harris, C. R., Millman, K. J., van der Walt, S. J., et al. 2020, Natur, 585, 357
Helling, C., Ackerman, A. S., Allard, F., et al. 2008, MNRAS, 391, 1854
Hinkley, S., Carter, A. L., Ray, S., et al. 2022, PASP, 134, 095003
Hunter, J. D. 2007, CSE, 9, 90
Karalidi, T., Apai, D., Marley, M. S., & Buenzli, E. 2016, ApJ, 825, 90
Karalidi, T., Apai, D., Schneider, G., Hanson, J. R., & Pasachoff, J. M. 2015, ApJ, 814, 65
Kass, R. E., & Raftery, A. E. 1995, Journal of the American Statistical Association, 90, 773
Lew, B. W. P., Apai, D., Marley, M., et al. 2020, ApJ, 903, 15
Lew, B. W. P., Apai, D., Zhou, Y., et al. 2016, ApJL, 829, L32
Lew, B. W. P., Apai, D., Zhou, Y., et al. 2020, AJ, 159, 125
Lomb, N. R. 1976, Ap&SS, 39, 447
Luger, R., Agol, E., Foreman-Mackey, D., et al. 2019, AJ, 157, 64
Manjavacas, E., Apai, D., Zhou, Y., et al. 2017, AJ, 155, 11
Marley, M. M. S. M., Ackerman, A. A. S., Cuzzi, J. N. J., & Kitzmann, D. 2013, in Comparative Climatology of Terrestrial Planets, Part III: Clouds and Hazes, ed. S. J. Mackwell et al. (Tucson, AZ: Univ. Arizona Press), 367
Marley, M. S., Seager, S., Saumon, D., et al. 2002, ApJ, 568, 335
Marois, C., Macintosh, B., Barman, T., et al. 2008, Sci, 322, 1348
Marois, C., Zuckerman, B., Konopacky, Q. M., Macintosh, B., & Barman, T. S. 2010, Natur, 468, 1080
Metchev, S. A., Heinze, A., Apai, D., et al. 2015, ApJ, 799, 154
Miles, B. E., Skemer, A. J., Barman, T. S., Allers, K. N., & Stone, J. M. 2018, ApJ, 869, 18
Miles, B. E., Skemer, A. J. I., Morley, C. V., et al. 2020, AJ, 160, 63
Miles-Páez, P. A. 2021, A&A, 651, L7
Millar-Blanchaer, M. A., Girard, J. H., Karalidi, T., et al. 2020, ApJ, 894, 42
Morley, C. V., Marley, M. S., Fortney, J. J., & Lupu, R. 2014, ApJL, 789, L14
Mukherjee, S., Fortney, J. J., Jensen-Clem, R., et al. 2021, ApJ, 923, 113
Newville, M., Stensitzki, T., Allen, D. B., & Ingargiola, A. 2014, LMFIT: Non-Linear Least-Square Minimization and Curve-Fitting for Python, Zenodo, doi:10.5281/zenodo.11813
Plummer, M. K., & Wang, J. 2022, ApJ, 933, 163
Radigan, J., Jayawardhana, R., Lafrenière, D., et al. 2012, ApJ, 750, 105
Rameau, J., Chauvin, G., Lagrange, A. M., et al. 2013, ApJL, 772, L15
Rhines, P. B. 1975, JFM, 69, 417
Rich, E. A., Currie, T., Wisniewski, J. P., et al. 2016, ApJ, 830, 114
Robinson, T. D., & Marley, M. S. 2014, ApJ, 785, 158
Robitaille, T. P., Tollerud, E. J., Greenfield, P., et al. 2013, A&A, 558, A33
Scargle, J. D. 1982, ApJ, 263, 835
Scholz, A., Kostov, V., Jayawardhana, R., & Mužić, K. 2015, ApJL, 809, L29
Showman, A. P., & Guillot, T. 2002, A&A, 385, 166
Showman, A. P., & Kaspi, Y. 2013, ApJ, 776, 85
Showman, A. P., Tan, X., & Parmentier, V. 2020, SSRv, 216, 139

Showman, A. P., Tan, X., & Zhang, X. 2019, ApJ, 883, 4
Stone, J. M., Skemer, A. J., Kratter, K. M., et al. 2016, ApJL, 818, L12
STScI Development Team 2013, pysynphot: Synthetic Photometry Software Package, Astrophysics Source Code Library, ascl:1303.023
Tan, X., & Showman, A. P. 2019, ApJ, 874, 111
Tan, X., & Showman, A. P. 2021a, MNRAS, 502, 678
Tan, X., & Showman, A. P. 2021b, MNRAS, 502, 2198
Tannock, M. E., Metchev, S., Heinze, A., et al. 2021, AJ, 161, 224
Tremblin, P., Phillips, M. W., Emery, A., et al. 2020, A&A, 643, A23
VanderPlas, J. T. 2018, ApJS, 236, 16
Virtanen, P., Gommers, R., Oliphant, T. E., et al. 2020, NatMe, 17, 261
Vos, J. M., Allers, K. N., & Biller, B. A. 2017, ApJ, 842, 78
Vos, J. M., Biller, B. A., Allers, K. N., et al. 2020, AJ, 160, 38
Vos, J. M., Faherty, J. K., Gagné, J., et al. 2022, ApJ, 924, 68
Wang, J. J., Gao, P., Chilcote, J., et al. 2022, AJ, 164, 143
Waskom, M. L. 2021, JOSS, 6, 3021
Yang, H., Apai, D., Marley, M. S., et al. 2014, ApJL, 798, L13
Yang, H., Apai, D., Marley, M. S., et al. 2016, ApJ, 826, 8
Zechmeister, M., & Kürster, M. 2009, A&A, 496, 577
Zhang, X., & Showman, A. P. 2014, ApJL, 788, L6
Zhang, Z., Liu, M. C., Claytor, Z. R., et al. 2021, ApJL, 916, L11
Zhou, Y., Apai, D., Lew, B. W. P., et al. 2019, AJ, 157, 128
Zhou, Y., Apai, D., Metchev, S., et al. 2018, AJ, 155, 132
Zhou, Y., Apai, D., Schneider, G. H., Marley, M. S., & Showman, A. P. 2016, ApJ, 818, 176
Zhou, Y., Bowler, B. P., Morley, C. V., et al. 2020, AJ, 160, 77